Effect of Non-linear Loading Paths on Sheet Metal Fracture: Large Strain In-plane Compression Followed by Uniaxial Tension

by

Stephane Marcadet

Ingénieur de l'Ecole Polytechnique (2010)

Submitted to the Department of Mechanical Engineering
in Partial Fulfillment of the Requirements for the Degree of

Master of Science in Mechanical Engineering

at the

Massachusetts Institute of Technology

February 2012

Signature of Author:______________________________
Department of Mechanical Engineering
January 27, 2012

Certified by:______________________________
Tomasz Wierzbicki
Professor of Applied Mechanics
Thesis Supervisor

Accepted by:______________________________
David E. Hardt
Professor of Mechanical Engineering
Chairman, Committee for Graduate Students

Effect of Non-linear Loading Paths on Sheet Metal Fracture: Large Strain In-plane Compression Followed by Uniaxial Tension

Stephane Marcadet

Submitted to the Department of Mechanical Engineering
on January 27, 2012, in partial fulfillment of the requirements for the degree of
Master of Science in Mechanical Engineering

Abstract

Advanced high strength steel sheets are rapidly entering the transport industry, as their high strength to weight ratio helps improving fuel and costs efficiency. The early ductile fracture of these materials limits their formability and crashworthiness. A phenomenological criterion to predict ductile fracture has been developed based on a law of damage accumulation weighted by the stress state. The calibration of such a model requires accurate measurements of the history of stress and strain state up to the onset of fracture. The phenomenon of localized necking occurs prior to ductile fracture in most types of loading of sheet metal. In order to measure the local state of stress and strain, a hybrid experimental and numerical method is tested. The Finite Element model can accurately predict the load displacement relation using a quadratic Hill 48 yield surface and an associated flow rule. The evolution of the local stresses and strains in the material are found to be non linear after necking. Results of such a method to calibrate the fracture criterion provide a validation of the model in a large range of loadings, including uniaxial, biaxial and shear.

The effect of a reverse loading is then explored by developing an innovative experimental procedure to adapt the hybrid method for in plane compression followed by uniaxial tension of sheet metal. An Anti Buckling Device (ABD) and special grips are developed to delay buckling of the sheet. The hybrid method requires an accurate constitutive model of the material in the case of reverse loading for the Finite Element model. A modified Yoshida hardening called IH + LK + LNK combining isotropic hardening, linear and non linear kinematic hardening provides good prediction of the load displacement relation. An analysis of the history of local stresses and strains up to the onset of fracture suggests that limited damage is accumulated during the compression phase, validating the phenomenological model.

Thesis Supervisor: Tomasz Wierzbicki

Title: Professor of Applied Mechanics

Table of Contents

List of figures

List of Tables

Chapter 1.

I. Introduction

1.1 Background

1.1.1 Ductile Fracture

The transportation industry is putting considerable recourses to integrate high strength to weight ratio materials in the vehicles structures in order to improve fuel and costs efficiency. Advanced high strength steel sheets play a major role as they provide very high strengths at reasonable weight. The use of these materials is restricted by low ductile fracture that limits their formability and crashworthiness (Fig. 1).

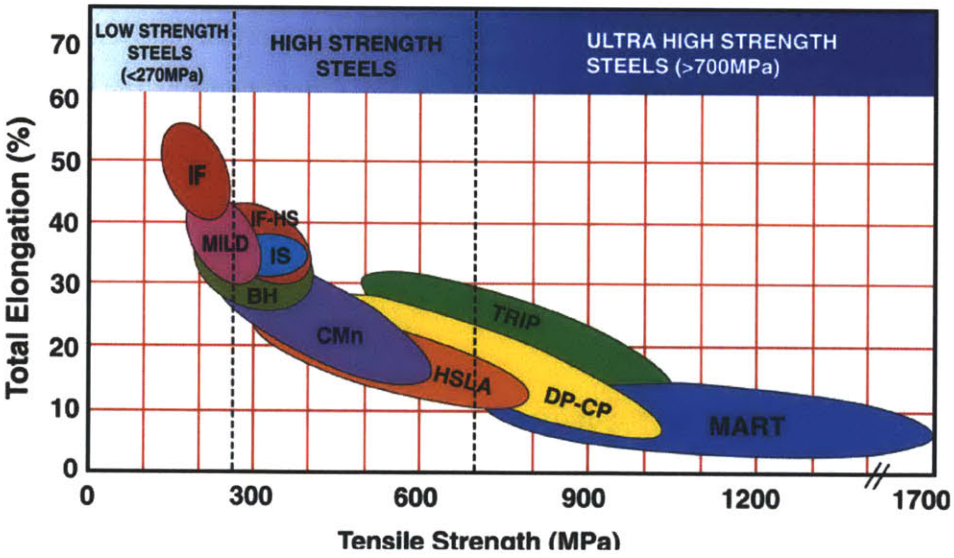

Figure 1Tensile strength versus total elongation plot of advanced high strength steels

Ductile fracture is often studied on a microscopic scale, focusing on the propagation of cracks. McClintock (1968) and Rice and Tracey (1969) were the first to show that the stress triaxiality governs the growth of voids in the material. Gurson (1977) introduced the void volume fraction as an internal variable in a porous plasticity model. A number of modified Gurson models have been developed since, introducing notions such as the void coalescence (Tvergaard and Needleman, 1984) and void shape effects (Pardoen and Hutchinson, 2000).

As an alternative, attempts to predict ductile fracture from a phenomenological point of view have been carried out. They are based on the assumption that the onset of fracture occurs when a certain critical value of the plastic strain is reached. An accumulation of the plastic strain weighted by a function of the stress state is introduced. This weight function has recently been proven to depend on the state of stress (Bao and Wierzbicki 2003, Wierzbicki and Xue 2005, Bai and Wierzbicki 2008). Two invariants of the stress of state, triaxiality and Lode angle are taken into account.

Hancock and McKenzie's (1976) tensile tests on axisymmetric notched specimens show that the ductility decreases with triaxiality, as predicted in Rice and Tracey's (1969) fracture model. Hancock and Brown (1983) compared tests on cylindrical and flat specimens and concluded that ductile fracture limits depend on the stress state and not the strain state. More recently, numerous innovative tests have been developed by Bao (2003), Mohr and Henn (2007) and Mohr and Oswald (2008) to explore the dependency of fracture in a wide range of stress states.

1.1.2 Cyclic plasticity models.

Kinematic hardening models are most commonly used for non-proportional monotonic loadings or cyclic loadings. Therefore they seem to be a good candidate for reverse loading. Kinematic hardening parameters are used as a back stress in the yield surface formulation.

The simplest kinematic hardening model is the linear kinematic hardening law introduced by Prager (1949). In this case, the back stress evolution is unbounded and evolves along the direction of the plastic strain increment.

But linearity is rarely observed in the stress strain response. That is why a more complex kinematic hardening model is proposed by Armstrong and Frederick (1966, 2007), introducing a second term, the recall term, which activates the so called dynamic-recovery. The recall term is collinear with the back stress and is proportional to the equivalent plastic strain rate. As a result, the evolution of the back stress is no longer linear and unbounded and converges towards a saturation value under monotonic loading. As discussed by Lemaitre and Chaboche (1994), the dynamic recovery term may be interpreted as a description of the "fading memory effect of the strain path." For example, in the case of uniaxial tension, the back stress evolution asymptotically approaches a saturation value.

As an even better approximation, several such models can be added with different recall constants to form the total back stress (Chaboche et al., 1979; Chaboche and Rousselier, 1983). The use of a non linear kinematic hardening gives good prediction in the case of a cyclic loading in the range of small strains, as it is able to describe the Bauschinger effect. As a particular case of the superposition of back stresses technique, a model coupling a linear kinematic hardening and a non linear kinematic hardening gives better results in the case of mid and high strains as it describes the permanent softening behavior during reverse deformation, especially with advanced high strength steels with almost no workhardening stagnation (Yoshida et al., 2002)..

1.1.3 In-plane compression experiments for sheet materials

In order to test reverse uniaxial loading of sheet metal, in-plane compression has to be performed experimentally. This implies some technical difficulties to avoid elastic or plastic buckling of the specimens in the range of small strains. A design has originally been developed by Dietrich and Turski (1978) to compress sheet metal. Kuwabara (1995) et al. introduced an Anti Buckling Device used with a lateral blank holder to apply a pressure reaching 1% of the elastic limit. In another attempt, Yoshida et al. tried to stack several dogbone specimens to delay buckling. The stack is maintained by adhesive and placed in an anti buckling device applying up to 10% of compressive strain. Boger et al. apply a lateral pressure to the specimens using a hydraulic system through clamping plates. Several methods to take frictional effects into account have been developed. The geometry of the specimen plays a major role in the efficiency of these experimental procedures. A double wedge system using Teflon sheets of thickness of half a millimeter has been introduced by Cao et al., providing an elastic support to the specimen.

1.1.4 Reverse loading fracture experiments

The effects of reverse loading have not yet been fully understood and explained. McClintock (1993) explained that crack nucleation can be caused by strain concentration under cyclic loading. Seok et al. (1999) showed that the fracture resistance curves decreases with decreasing minimum-to-maximum load ratio of cyclic loading and decreasing incremental plastic displacement. Harvey (2000) performed strain controlled cycling followed by monotonic tensile loading to fracture. He found by looking at the fracture surface using scanning electron microscopy (SEM) that cyclic loading increased the total number of micro voids. The aspect ratio of micro voids seemed to be only a function of the loading and showed no dependency on pre strain. Other studies were mostly focused on the effect of preloading on fracture toughness and propagation. Some studies investigated the effect of reverse loading on ductile propagation of cracks in the case of reverse bending tests of beams. Bao and Treitler (2004) investigated the effect of reverse loading on crack formation. Notched cylindrical tensile specimens have been adapted to perform compression tension tests. They proved that the pre-compression plays a very important role in the crack formation. The dimple structure observed from fracture surface is finer and the size of voids is smaller in the case of pre-compression. Particles crack along the loading direction under pre-compression loading, while particles fail in the direction perpendicular to the loading direction under tensile loading.

1.2 Objectives of this thesis

The objective of this study is to understand the effect of complex non linear quasi-static loadings on the onset of ductile fracture of advanced high strength steel sheets. The first step is the validation, in the case of a dual-phase steel, of an innovative hybrid experimental and numerical method developed by Dunand and Mohr (2010). This method is then adapted to evaluate the effect of reverse loading on ductile fracture of sheet metal.

The hybrid method is used to characterize the ductile fracture as a function of the stress and strain state. Several types of tests are performed to observe fracture in a wide range of stress states: tensile notched- shaped specimens and a tensile specimen with a central hole, a shear test and a punch test. Most phenomenological fracture criterions require the identification of the history of equivalent plastic strain and stress state. These quantities cannot be directly measured on the experiment. Therefore, a Finite Element analysis of these tests provides the history of triaxiality, Lode angle parameter and equivalent plastic strain. The local stress and strain state evolution is non linear because of the localization of the plastic strain that leads to the necking effect. A phenomenological criterion known as the Modified Mohr Coulomb criterion to predict the quasi static ductile fracture of Advanced High Strength Steel sheets is calibrated and validated for these tests.

In the second part, an experimental technique of a pre compression on tensile specimens of sheet metal is presented. It uses an anti buckling device and special grips. Large in plane pre-compression followed by uniaxial tension tests to fracture have been performed for various levels of pre strain. A suitable plasticity model for large in plane reverse deformations is carefully developed to predict the behavior of the material. The hybrid experimental and numerical method is used to observe the history of local state of stress and strain at the fracture locus for all tests. It is found that pre compression has an important effect on the equivalent strain at fracture, but has little effect on the stress state at fracture. It is interpreted that, in the frame of the phenomenological theory of damage accumulation, little damage is accumulated during the compression phase.

1.3 Material

The detailed calibration of the Modified Mohr Coulomb criterion has been performed on a Dual-Phase steel. Its mechanical characteristics are presented in details in the following study. Sheets have a thickness of 1.44 mm.

The study of the effect of reverse loading on ductile fracture has been performed on a different Dual-Phase steel, DP780, provided by US Steel (Fig. 2). Its Young modulus is 195 GPa. Its yield point is different in tension (450 MPa) and compression (510 MPa). This is due to the rolling treatment. In order to take this particularity into account, an initial value for the back stress is introduced in the plasticity model. The Lankford coefficients have been measured for this material to be able to take its anisotropy into account. Sheets have a thickness of 1.06 mm.

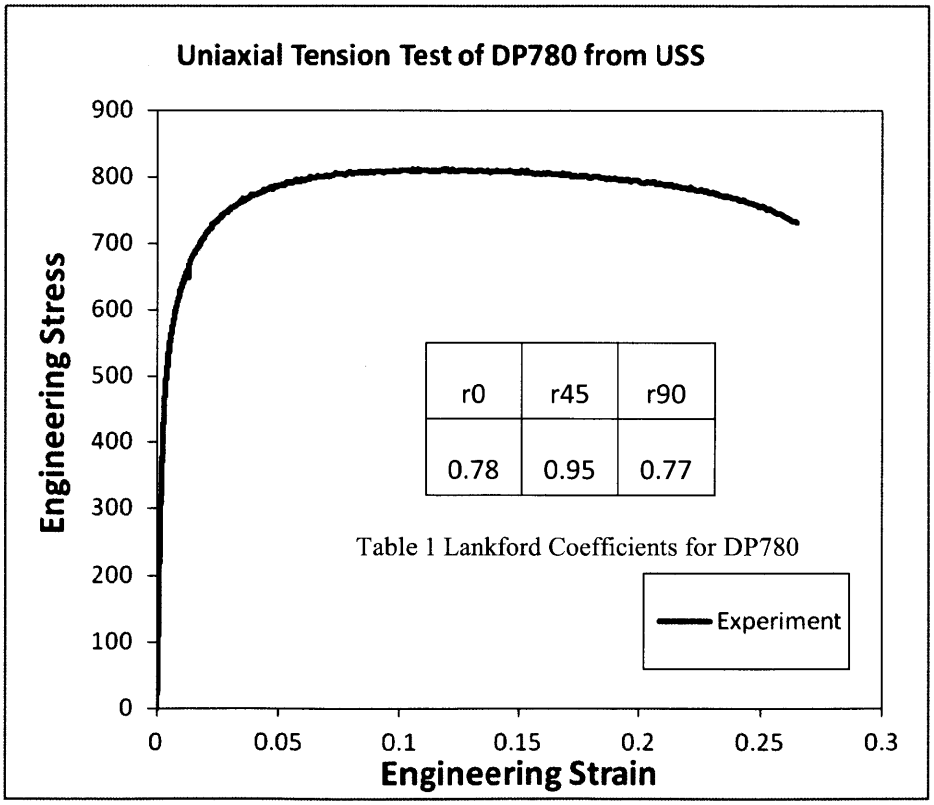

r0	r45	r90
0.78	0.95	0.77

Table 1 Lankford Coefficients for DP780

Figure 2 Uniaxial Tension test of DP780 from USS in 0 direction

Chapter 2.

II Plasticity & Fracture Models

A good understanding and modeling of the plastic behavior of the material is a necessary step towards the study of ductile fracture. Simulating the experiments in Finite Element Analysis software provides the history of the stress state and local strains during the different loading phases. The interests of this analysis are the triaxiality, load angle and local equivalent plastic strain in the elements where experimental fracture is expected to occur first. Simulation is considered as relevant if the load-displacement curves of the experiment and its computer simulation match. Therefore the measurement of these parameters is highly dependent on the plasticity model. That is why an accurate plasticity model is crucial as the damage accumulation law is based on these parameters.

2.1 Plasticity model for linear loading paths

The Finite Element Analysis requires the determination of the plastic behavior of the material. According to Mohr at al. (2010), a standard plasticity model can be used for advanced high strength steels, featuring an anisotropic quadratic yield surface (Hill 1948), an associated flow rule and an isotropic hardening law.

2.1.1 Plasticity Model

Hill 48 quadratic yield surface:

$$f\left(\underline{\sigma}, \underline{\varepsilon}^{pl}\right) = \bar{\sigma} - k\left(\underline{\varepsilon}^{pl}\right) = 0 \tag{1}$$

The Hill stress $\bar{\sigma}$ is defined by:

$$\bar{\sigma} = \sqrt{\underline{\underline{P}}(\underline{\sigma}) : \underline{\sigma}} \tag{2}$$

The stress state $\underline{\sigma}$ vector is written using an engineering notation:

$$\underline{\sigma} = [\sigma_{11}, \sigma_{22}, \sigma_{33}, \sigma_{11}, \sigma_{12}, \sigma_{23}] \tag{3}$$

The matrix $\underline{\underline{P}}$ can be determined experimentally, and expressed in terms of the Lankford coefficients.

Associated flow rule:

$$d\underline{\varepsilon}^{pl} = d\lambda \frac{\partial \bar{\sigma}}{\partial \underline{\sigma}} \tag{4}$$

Isotropic hardening law:

$$dk = H(\bar{\varepsilon}^{pl}) d\bar{\varepsilon}^{pl} \tag{5}$$

where the equivalent plastic strain $\bar{\varepsilon}^{pl}$ defined by:

$$\bar{\varepsilon}^{pl} = \bar{\varepsilon}^{pl}{}_0 + \int_0^t \dot{\bar{\varepsilon}}^{pl} dt \tag{6}$$

and $\bar{\varepsilon}^{pl}{}_0$ is the initial equivalent plastic strain.

The equivalent strain rate is given by:

$$\dot{\bar{\varepsilon}}^{pl} = \sqrt{\underline{\dot{\varepsilon}^{pl}} . \underline{\dot{\varepsilon}^{pl}}} \tag{7}$$

2.1.2 Plasticity calibration

The determination of the hardening law can be done by identifying the stress-strain curve when performing uniaxial tension tests. Dogbone specimens are cut out of stell sheets using the abrasive waterjet machine. All specimens were tested to fracture on an MTS 200 kN electromechanical load frame equipped with a 200 kN load cell and wedge grips. Displacements are measured by a Digital Image Correlation (DIC) software called VIC-2D. The deformed images are compared to the undeformed one using virtual extensometers that give the relative displacements of two points on a vertical line as well as two points on a horizontal line. The specimens must first be painted in white, then black paint is sprayed to provide good contrast.

In order to determine the anisotropy of the material, specimens are cut from sheets along three different directions in relation to the orientation of the material (rolling, cross rolling, 45 degrees, Fig. 3-4). This allows us to determine plastic anisotropy characterized by the P matrix in the yield surface definition.

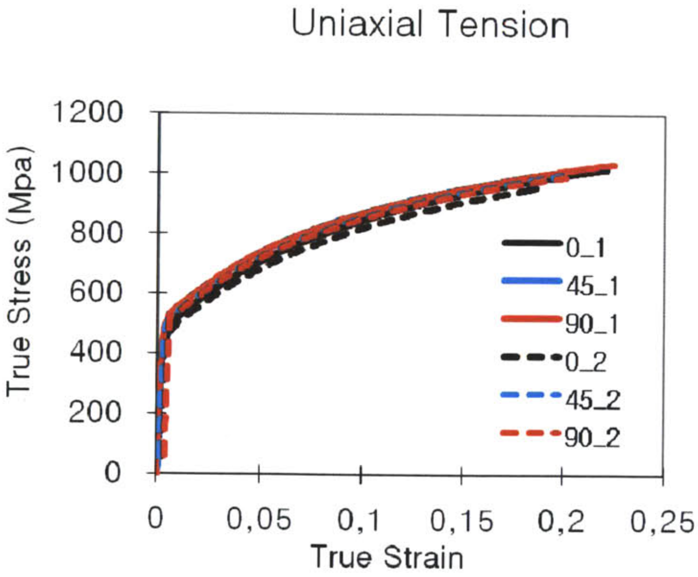

Figure 4 Uniaxial Tension tests of Dual Phase Steel in three directions to rolling direction

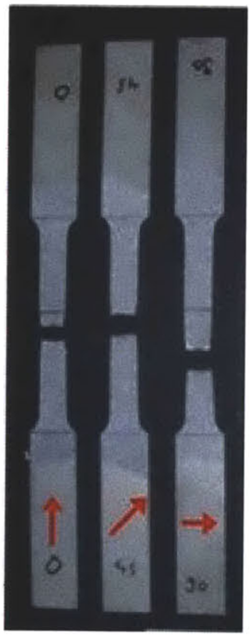

Figure 3 Dogbone specimens

When the maximum load is reached, localization of the strain occurs and the effect of necking makes it impossible to determine directly the hardening law for further strain level. As high levels of strain are reached, large deformation theory is used, where substantial differences between engineering and true stress and strain exist. As a consequence, true stress and strains will always be used in this study.

Engineering Longitudinal and Width strain is defined as below:

$$\varepsilon_L^{eng} = \frac{L}{L_0} \tag{8}$$

where L is the current length of the extensometer in the direction of the specimen and L_0 its initial length.

$$\varepsilon_W^{eng} = \frac{W}{W_0} \tag{9}$$

where W is the current length of the extensometer in the width direction and W_0 its initial length.

True strains before necking are then calculated from the engineering strains:

$$\varepsilon_{L,W}^{t} = \ln\left(1 + \varepsilon_{L,W}^{eng}\right) \tag{10}$$

Engineering stress is defined as below:

$$\sigma^{eng} = \frac{F}{A_0} \tag{11}$$

where A_0 is the surface of the specimen perpendicular to the tensile direction.

The true stress before necking is then found from:

$$\sigma^{t} = \sigma^{eng}\left(1 + \varepsilon_L^{eng}\right) \tag{12}$$

Strain in the third direction cannot be found from DIC but can be found assuming the incompressibility of the material:

$$\varepsilon_T^t = -\varepsilon_L^t - \varepsilon_W^t \tag{13}$$

Lankford coefficients are used to characterize the anisotropy of the plasticity through the yield surface. The Lankford coefficients are defined by:

$$r_\alpha = \frac{\varepsilon_W^t}{\varepsilon_T^t} \tag{14}$$

where α is the orientation of the specimen in relation to the rolling direction.

The Lankford coefficient corresponds to the slope of the curve showing the evolution of the true width strain as a function of the transverse strain. The curve has been plotted for the three specimens (Fig. 5). The fact that the Lankford parameter is not unity and not equal for all directions implies that the material is anisotropic (Fig. 6 & Table 2).

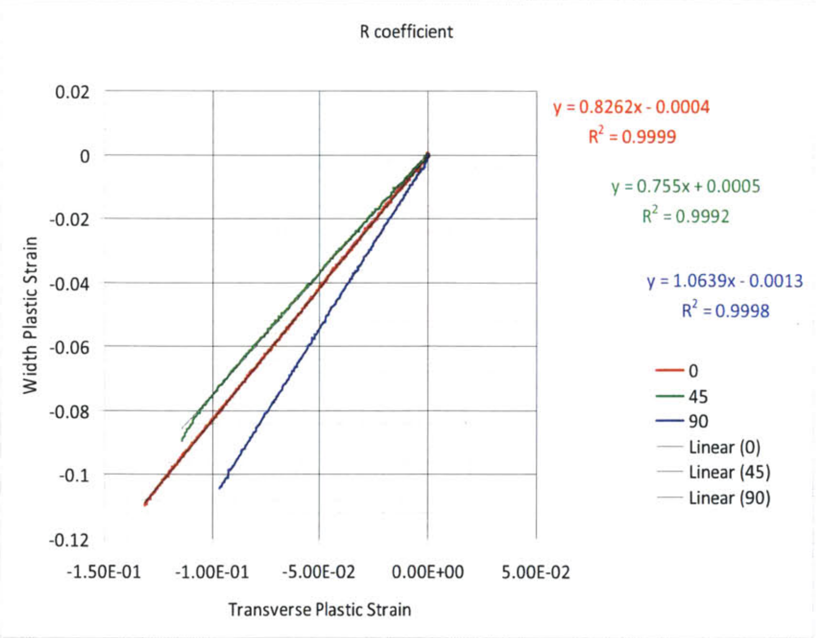

Figure 5 Diagram of evolution of width and transverse strain for Lankford coefficients determination

r0	r45	r90
0.82	0.755	1.064

Table 2 Lankford Coefficients

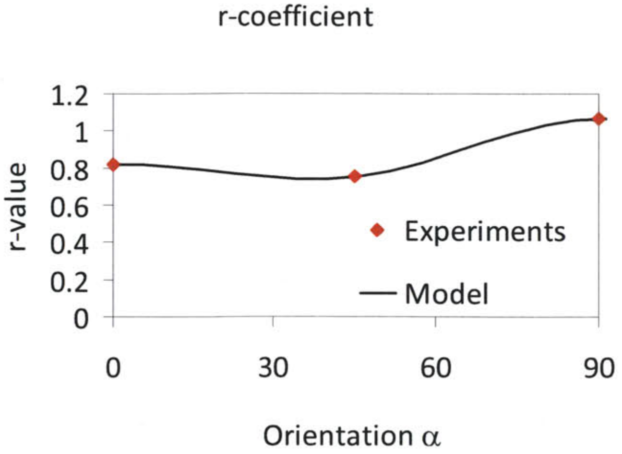

Figure 6 According to Mohr at al. (2010), the Lankford r coefficient can be plotted as a function of the α orientation from 0 to 90 degrees, knowing only the three coefficients in the 0, 45 and 90 degrees directions. An obvious anisotropy can be observed.

As the hardening law has only been determined experimentally in a range of strains up to the level reached at the maximum load in the uniaxial tensile test (0.2), an extrapolation is necessary to determine the mechanical behavior in a much higher range of strains.

A power law is being used in this study.

$$\sigma = A\bar{\varepsilon}^{p^n} \tag{15}$$

In other words, the hardening law is written as:

$$H(\bar{\varepsilon}^p) = An(\bar{\varepsilon}^p)^{n-1} \tag{16}$$

The method of least squares (in Excel: function trend line) is used to determine the two parameters of the power law before necking (Fig.7). This analytical law can be then plotted for a large range of strains. Typically, 0.9 has shown to be the maximum strain observed is this study. A discrete model is then chosen, and the points that correspond to a higher strain than that of the maximum load of uniaxial tensile tests has been adapted to fit the plasticity validation (Fig. 7 & table No. 4).

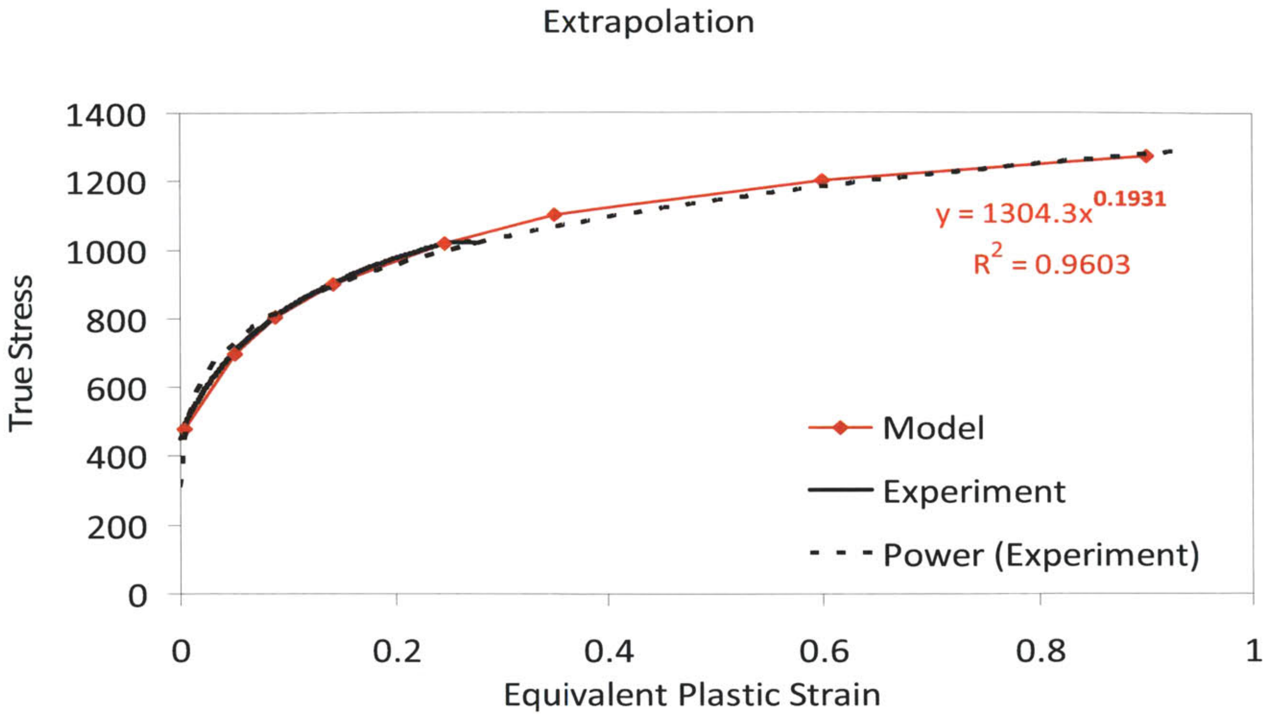

Figure 7 Interpolation, extrapolation, and discretization of the stress strain curve.

In Abaqus, the behavior of the material in the elastic range is specified by the Young modulus and Poisson ratio.

$$E = 200\ GPa$$

$$\nu = 0.3$$

The discrete model corresponding to the power law characterizing the hardening is written in the plastic section. A potential is then added, the coefficient of which are computed from the previously determined Lankford coefficients. According to the Abaqus analysis user's manual:

$$R_{22} = \sqrt{\frac{r_y(r_x+1)}{r_x(r_y+1)}}, \qquad R_{33} = \sqrt{\frac{r_y(r_x+1)}{(r_x+r_y)}}. \quad R_{12} = \sqrt{\frac{3(r_x+1)r_y}{(2r_{45}+1)(r_x+r_y)}}.$$

Stress	Equivalent Plastic Strain
480	0.004
695	0.05
805	0.088
900	0.141
1016	0.246
1100	0.35
1200	0.6
1250	0.9

Table 4 Yield surface anisotropy.

R22	**R33**	**R12**
1.067	**1.0138**	**1.108**

Table 3 Yield Surface anisotropy in Abaqus

2.2 Constitutive modeling for reverse loading

The plasticity model presented above has been tested in the case of reverse loading experiments. An isotropic hardening plasticity model fails to describe the Bauschinger effect that can be observed when performing a Finite Element analysis of a test applying compression followed by uniaxial tension to DP780 sheet metal (Fig. 8).

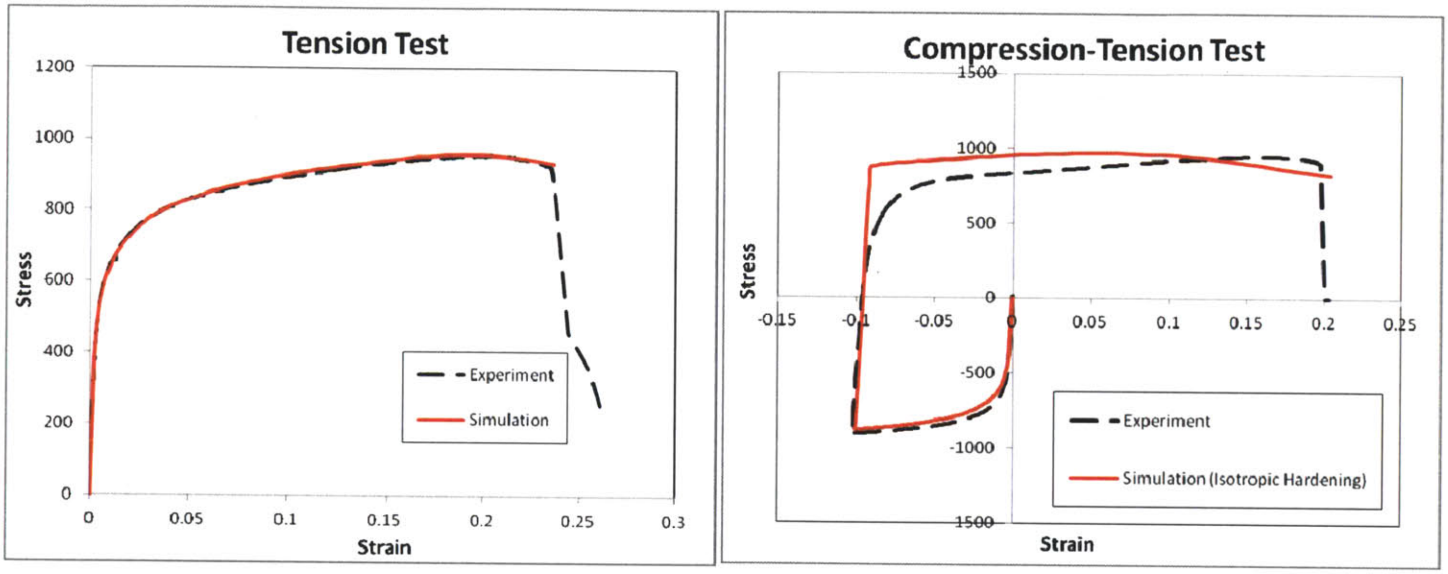

Figure 8 Comparison of Load Displacement prediction with Isotropic Hardening in the case of linear and reverse loading

A phenomenological model is developed to describe the large deformation behavior of the advanced high strength steel under static loading. In the following, we outline the rate independent finite strain constitutive equations, which involve the yield surface, flow rule, isotropic hardening law and kinematic hardening law. Double-underscored Bold upper case letters (e.g. $\underline{\underline{\mathbf{B}}}$) and lower case bold letters (e.g. $\underline{\underline{\mathbf{b}}}$) are used to denote matrices and tensors, while single-underscored bold lowercase letters (e.g. $\underline{\mathbf{b}}$) are used to denote vectors. Square brackets are exclusively used to indicate the arguments of a function, while round and curly brackets are employed to signify the precedence of mathematical operations.

2.2.1 Kinematics of finite strain

The constitutive model is implemented in the commercial finite element software Abaqus/explicit. Therefore, the standard finite strain formulation for 3D elements is used (Abaqus, 2008). The Cauchy stress tensor in the current configuration is denoted as $\underline{\underline{\boldsymbol{\sigma}}}$, while $d\underline{\underline{\boldsymbol{\varepsilon}}}$ denotes the work-conjugate strain increment. Stress and strain components, σ_{ij} and ε_{ij} , are reported in the current material coordinate systems, assuming that the orthotropic material symmetry is preserved throughout loading. Formally, we write

$$\underline{\underline{\boldsymbol{\sigma}}} = \sigma_{ij}(\mathbf{R}\mathbf{e}_i \otimes \mathbf{R}\mathbf{e}_j)\,, \tag{17}$$

with $\mathbf{R}$ denoting the rotation of the co-rotational material coordinate system; the unit vectors $\mathbf{e}_1$ and $\mathbf{e}_2$ are aligned with the initial rolling and cross-rolling directions.

2.2.2 Yield surface

The comparison of newly developed biaxial experiments (Mohr and Oswald, 2008) on advanced high strength steel sheets (dual phase steel DP590 and the TRIP-assisted steel TRIP780) with the simulation results shows that the associated orthotropic Hill (1948) plasticity model provides a satisfactory description of the large deformation response under multi-axial loading. According to C. Walters Ph.D. thesis, using the same testing technique, both Von Mises and Hill 1948 quadratic yield functions can adequately characterize the material used in this study (dual phase steel DP780) for in-plane properties, but only the Hill 1948 model was able to capture the reduction in thickness due to tensile strain.

The initial yield surface is defined as

$$f = \bar{\sigma} - k = 0\,, \tag{18}$$

where $\bar{\sigma} = \bar{\sigma}[\underline{\underline{\boldsymbol{\sigma}}}]$ defines the equivalent stress, k is the deformation resistance, and $\underline{\underline{\boldsymbol{\sigma}}}$ is the Cauchy stress tensor. The Hill'48 equivalent stress is typically given in the form

$$\bar{\sigma} = \sqrt{F(\sigma_{22}-\sigma_{33})^2 + G(\sigma_{33}-\sigma_{11})^2 + H(\sigma_{11}-\sigma_{22})^2 + 2L\sigma_{12}^2 + 2M\sigma_{13}^2 + 2N\sigma_{32}^2}, \qquad (19)$$

where F, G, H, L, M, and N are the coefficients describing the material anisotropy. In the present model, we introduce a deviatoric back stress tensor $\underline{\underline{\boldsymbol{\alpha}}}$, and replace the components σ_{ij} in Eq. (19) by $\sigma_{ij} - \alpha_{ij}$.

This gives the following expressions:

$$\underline{\underline{\boldsymbol{\xi}}} = \underline{\underline{\boldsymbol{\sigma}}} - \underline{\underline{\boldsymbol{\alpha}}} \qquad (20)$$

This quadratic form can be rewritten in a matrix form thanks to the fourth order tensor operator **P**.

$$\bar{\sigma} = \sqrt{(\underline{\underline{\boldsymbol{\sigma}}}) : \underline{\underline{\underline{\underline{\mathbf{P}}}}} : (\underline{\underline{\boldsymbol{\sigma}}})} \qquad (21)$$

$$\bar{\sigma} = \sqrt{\underline{\underline{\boldsymbol{\xi}}} : \underline{\underline{\underline{\underline{\mathbf{P}}}}} : \underline{\underline{\boldsymbol{\xi}}}} \qquad (22)$$

2.2.3 Associated flow rule

An associated flow rule is chosen to describe the evolution of the plastic strain tensor. Therefore, the increment in plastic strains, $d\underline{\underline{\boldsymbol{\varepsilon}}}^p$, is proportional to the derivative of the equivalent stress,

$$d\underline{\underline{\boldsymbol{\varepsilon}}}^p = d\lambda \frac{\partial \bar{\sigma}}{\partial \underline{\underline{\boldsymbol{\sigma}}}} \qquad (23)$$

where $d\lambda \geq 0$ is the plastic multiplier. The integral $\bar{\varepsilon}_p = \int d\lambda$ is referred to as the equivalent plastic strain.

Taking the deviatoric back stress into account and using the matrix form, the flow rule can be rewritten as follows:

$$d\underline{\underline{\boldsymbol{\varepsilon}}}^{p} = d\lambda \frac{\partial \overline{\sigma}}{\partial \underline{\underline{\boldsymbol{\xi}}}} \tag{24}$$

With:

$$\frac{\partial \overline{\sigma}}{\partial \underline{\underline{\boldsymbol{\xi}}}} = \frac{\underline{\underline{\underline{\underline{\mathbf{P}}}}}\,\underline{\underline{\boldsymbol{\xi}}}}{\overline{\sigma}} \tag{25}$$

2.2.4 Linear Kinematic hardening

The linear kinematic hardening rule is written as

$$d\underline{\underline{\boldsymbol{\alpha}}}_{1} = \frac{2}{3} c_{L}\, d\underline{\underline{\boldsymbol{\varepsilon}}}^{p}, \tag{26}$$

where c_L is a material parameters. It corresponds to the linear kinematic hardening law by Prager (1949); in this case, the back stress evolution is unbounded and evolves along the direction of the plastic strain increment.

2.2.5 Non Linear Kinematic hardening

The non-linear kinematic hardening rule is written as

$$d\underline{\underline{\boldsymbol{\alpha}}}_{2} = \frac{2}{3} c_{NL}^{1}\, d\underline{\underline{\boldsymbol{\varepsilon}}}^{p} - c_{NL}^{2}\, \underline{\underline{\boldsymbol{\alpha}}}_{2}\, d\lambda, \tag{27}$$

where c_{NL}^{1} and c_{NL}^{2} are material parameters. This second term of the kinematic hardening activates the dynamic-recovery term proposed by Armstrong and Frederick (1966, 2007). As a result, the evolution of the back stress is no longer unbounded and converges towards a saturation value under monotonic loading. As discussed by Lemaitre and Chaboche (1994), the dynamic recovery term may be interpreted as a description of the "fading memory effect of the strain path." For example, in the case of uniaxial tension, the back stress evolution asymptotically approaches a saturation value.

2.2.6 Isotropic hardening

In addition to a kinematic hardening law, an isotropic hardening law is used to describe the evolution of the deformation resistance k during plastic loading. It is assumed that the deformation resistance depends on the evolution of the equivalent plastic strain. We write

$$dk = H_{\varepsilon} d\bar{\varepsilon}^{p}, \tag{28}$$

where $d\bar{\varepsilon}^{p}$ is the increment in the equivalent plastic strain. The deformation resistance is an exponential function of the equivalent plastic strain,

$$k = k_0 + H_0 \{1 - \exp[-A\bar{\varepsilon}^{p}]\}, \tag{29}$$

with the model parameters k_0, H_0, and A. Consequently, the relationship for the isotropic strain hardening modulus reads

$$H_{\varepsilon}[\bar{\varepsilon}^{p}] = \frac{dk}{d\bar{\varepsilon}^{p}} = AH_0 \exp[-A\bar{\varepsilon}^{p}]. \tag{30}$$

2.2.7 Plasticity model parameter identification

The Calibration of the Hill surface is performed by measuring the lankford coefficients characterizing the anisotropy of the material.

The initial yield point k_0 has been found to be different in compression and tension. Therefore an initial back stress has to be determined to take this asymmetry into account, and k_0 is taken as the average of the yield point in tension Y_1 and the yield point in compression Y_2.

According to Beese and Mohr (2011), the back stress induced by the rolling procedure should have the following form:

$$\underline{\underline{\alpha}}_0 = \begin{bmatrix} \alpha & 0 & 0 \\ 0 & 0 & 0 \\ 0 & 0 & -\alpha \end{bmatrix}. \tag{31}$$

The tensor is written so that the first direction corresponds to the rolling direction, and the third to the through thickness direction.

The main goal of the numeric model is to be able to predict the stress and strain state up to fracture at the fracture locus. Therefore, the behavior of the material must remain accurately predicted after the onset of the necking phase. It is not possible to determine experimentally suitable values for the plasticity model parameters that allow us to predict the load displacement relation after the onset of the necking phase. In these conditions, the calibration of the IH + LK + NLK hardening model, using 5 parameters, requires us to use an optimization method.

An order of magnitude for the parameters can be estimated by looking at the asymptotic behavior of the material at very large deformation.

Alternatively, a simplified 1D model for uniaxial tests is first implemented in order to have a first guess on the seeds values for the modified Yoshida model. The computationally efficient method allows us to use a Monte Carlo method to look for the coefficients. For each parameter in the model, a certain domain delimited in a minimum and a maximum possible value is guessed, according to the expected result. The load displacement predicted by the 1D model is compared to the experimental load displacement relation for each compression tension test. This comparison can only be done up to the point corresponding to maximum load, as the 1D model becomes irrelevant after the onset of diffused necking. The set of parameters which minimizes the area between the experimental and predicted stress strain curve is kept as seed values for the main optimization procedure.

In order to carefully optimize the parameters of the plasticity model, an inverse calibration using Finite Element Analysis is performed. In order to determine a suitable set of parameters, an objective function defined by the error between the experimental and numerically predicted load displacement relation is introduced.

$$[C,\gamma,H,Q,b] = \arg\min_{C,\gamma,H,Q,b} \sum_{Tests} \left\| F^{FEA}(u) - F^{EXP}(u) \right\| \tag{32}$$

This is an unconstrained non-linear optimization problem that can be solved using a derivative-free simplex algorithm. To solve this problem, the Matlab function “fminsearch” has been used. This function uses the Nelder-Mead method described by Lagarias et al. (1998). It requires introducing a coupling with Finite Element software (Abaqus) in order to be able to evaluate the objective function at each step of the optimization process.

2.3 Identification of the load path to fracture

Macroscopic ductile fracture models are based on a damage accumulation during the loading history. Bai and Wierzbicki (2008) conclude that this damage accumulation shows great dependency on some parameters of the stress state. The history of two stress invariants, triaxiality and Lode angle, play a major role.

2.3.1 Stress and Strain invariants

The Equivalent Plastic Strain $\bar{\varepsilon}^{pl}$ is defined by:

$$\bar{\varepsilon}^{pl} = \bar{\varepsilon}^{pl}{}_0 + \int_0^t \dot{\bar{\varepsilon}}^{pl} dt$$

where $\bar{\varepsilon}^{pl}{}_0$ is the Initial Plastic Strain.

The strain rate $\dot{\bar{\varepsilon}}^{pl}$ being:

$$\dot{\bar{\varepsilon}}^{pl} = \sqrt{\underline{\underline{\dot{\varepsilon}^{pl}}} : \underline{\underline{\dot{\varepsilon}^{pl}}}}$$

Triaxiality η is by definition:

$$\eta = \frac{-p}{q}$$

With the pressure p, Von Mises stress q and deviatoric stress $\underline{\underline{s}}$ are calculated as shown:

$$\begin{cases} p = \sigma_{ii} = tr\left(\underline{\underline{\sigma}}\right) \\ q = \sqrt{\frac{3}{2}\left(\underline{\underline{s}}:\underline{\underline{s}}\right)} \\ \underline{\underline{s}} = \underline{\underline{\sigma}} - p\underline{\underline{1}} \end{cases} \tag{33}$$

Triaxiality can be understood as a normalized pressure. It describes the average level of the stress and its distribution along the three principal directions.

The dimensionless Lode Angle parameter is defined by:

$$\bar{\theta} = 1 - \frac{2}{\pi}\arccos(\xi) \tag{34}$$

with ξ being :

$$\xi = \left(\frac{r}{q}\right)^3 \tag{35}$$

A coefficient α is now introduced:

$$\alpha = \frac{\sigma_{II} - \sigma_I}{\sigma_{III} - \sigma_I} \tag{36}$$

In other words, α is the relative position of the second principal stress between the two others. The Lode Angle is a function of α only:

$$\bar{\theta} = \bar{\theta}(\alpha) \tag{37}$$

According to the graph showing $\bar{\theta}$ as a function of α (Fig.10), $\bar{\theta}$ can be approximated with good accuracy thanks to the following formula:

$$\bar{\theta} \sim 1 - 2\alpha \tag{38}$$

The Lode angle must be interpreted as an indicator of the relative position of the second principal stress between the two other ones (Fig. 9).

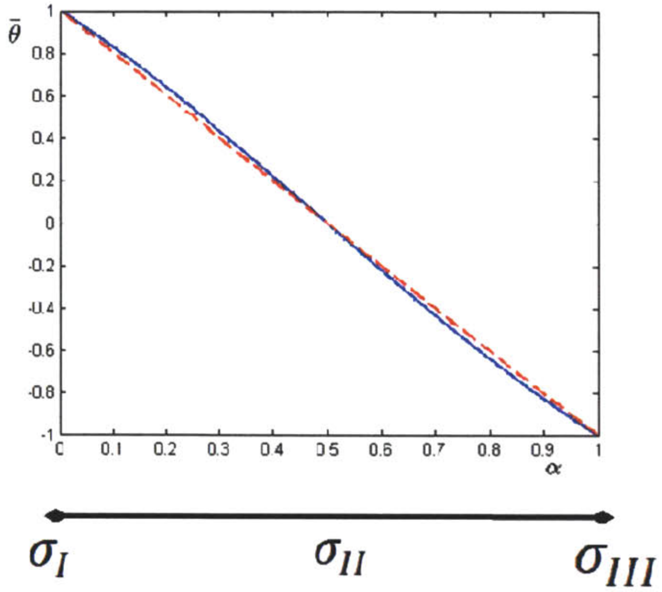

Figure 9 Interpretation of the Lode Angle in terms of principal stresses.

2.3.2 *Modified Mohr Coulomb Model for fracture*

The previous results indicate that a criterion to predict the fracture must take into account the history of the stress state during the loading.

Bai and Wierzbicki (2008) have modified the Mohr Coulomb criterion (MMC) to predict the fracture with a damage accumulation that takes the history of the state of stress into account.

The fracture locus for proportional loading is defined as:

$$\hat{\varepsilon}_f = \left\{ \frac{A}{c_2}\left[c_3 + \frac{\sqrt{3}}{2-\sqrt{3}}(1-c_3)\left(\sec\left(\frac{\bar{\theta}\pi}{6}\right) - 1\right)\right]\left[\sqrt{\frac{1+c_1^2}{3}} \cos\left(\frac{\bar{\theta}\pi}{6}\right) + c_1\left(\eta + \frac{1}{3} \sin\left(\frac{\bar{\theta}\pi}{6}\right)\right)\right]\right\}^{-\frac{1}{n}} \qquad (39)$$

For non-proportional loading, linear incremental form of damage indicator D is:

$$D(\bar{\varepsilon}^p) = \int_0^{\bar{\varepsilon}^p} \frac{d\bar{\varepsilon}^p}{\hat{\varepsilon}_f(\eta,\bar{\theta})} \tag{40}$$

The fracture initiates when:

$$D(\bar{\varepsilon}^f) = 1 \tag{41}$$

It will be useful later in this study to introduce the plane stress 36 ondition $\sigma_{33} = 0$ n (Wierzbicki, Xue, 2005):

$$-\frac{27}{2}\bar{\eta}(\bar{\eta}^2 - \frac{1}{3}) = \sin(\frac{\pi}{2}\bar{\theta}) \tag{42}$$

where:

$$f_1 = \cos\left\{\frac{1}{3}\arcsin\left[-\frac{27}{2}\bar{\eta}(\bar{\eta}^2 - \frac{1}{3})\right]\right\} \tag{43}$$

$$\bar{\varepsilon}_f = \left\{\frac{A}{c_2} f_3\left[\left(\sqrt{\frac{1+c_1^2}{3}}\cdot f_1\right) + c_1\left(\bar{\eta} + \frac{f_2}{3}\right)\right]\right\}^{-\frac{1}{n}}$$

$$f_2 = \sin\left\{\frac{1}{3}\arcsin\left[-\frac{27}{2}\bar{\eta}(\bar{\eta}^2 - \frac{1}{3})\right]\right\} \tag{44}$$

$$f_3 = c_3 + \frac{\sqrt{3}}{2-\sqrt{3}}(1-c_3)(\frac{1}{f_1} - 1) \tag{45}$$

Chapter 3.

III Fracture experiments

3.1 Experiments

3.1.1 Specimens

Several different specimens are tested in order to study the fracture in a large range of states of stress both in terms of triaxiality and Lode angle. Various shapes of specimens for testing in a tensile machine are used because they are easy to perform and require universal testing equipment that is available in the industry. Notched specimens are used because the location of the onset of fracture always is know a priori (where the width is the smallest) and various histories of triaxiality and Lode angle can be studied by designing different notch radii. The central hole specimen allows to keep an almost constant type of loading, very close to uniaxial tension, all the way to fracture, whereas the triaxiality of the notched tensile specimens always shift at a certain point to a value close to that of biaxial tension, depending on the radius.

The punch test presents an equibiaxial loading and is the only test that allows us to observe a negative Lode angle. requires two video cameras and calibration to observe the displacement in the 3D space. The shear test, performed thanks to the butterfly specimen, is also interesting, as it is the only test that shows triaxiality close to zero. It has been performed on a biaxial hydraulic Instron machine, using a 200kN load cell in the vertical direction and a 25kN load cell in the horizontal direction. A zero force loading in maintained on the tensile direction, and shear loading is imposed on the horizontal direction. In fact, central hole and shear tests are the only ones where fracture does not occur on a triaxiality close to 0.66, so they have critical importance to determine the effect of triaxiality on fracture.

Various types of specimens, that allow us to reach a large range of loading histories all the way to fracture, are needed to be able to observe a dependency of the fracture locus on the type of loading and state of stress. (Fig. 10)

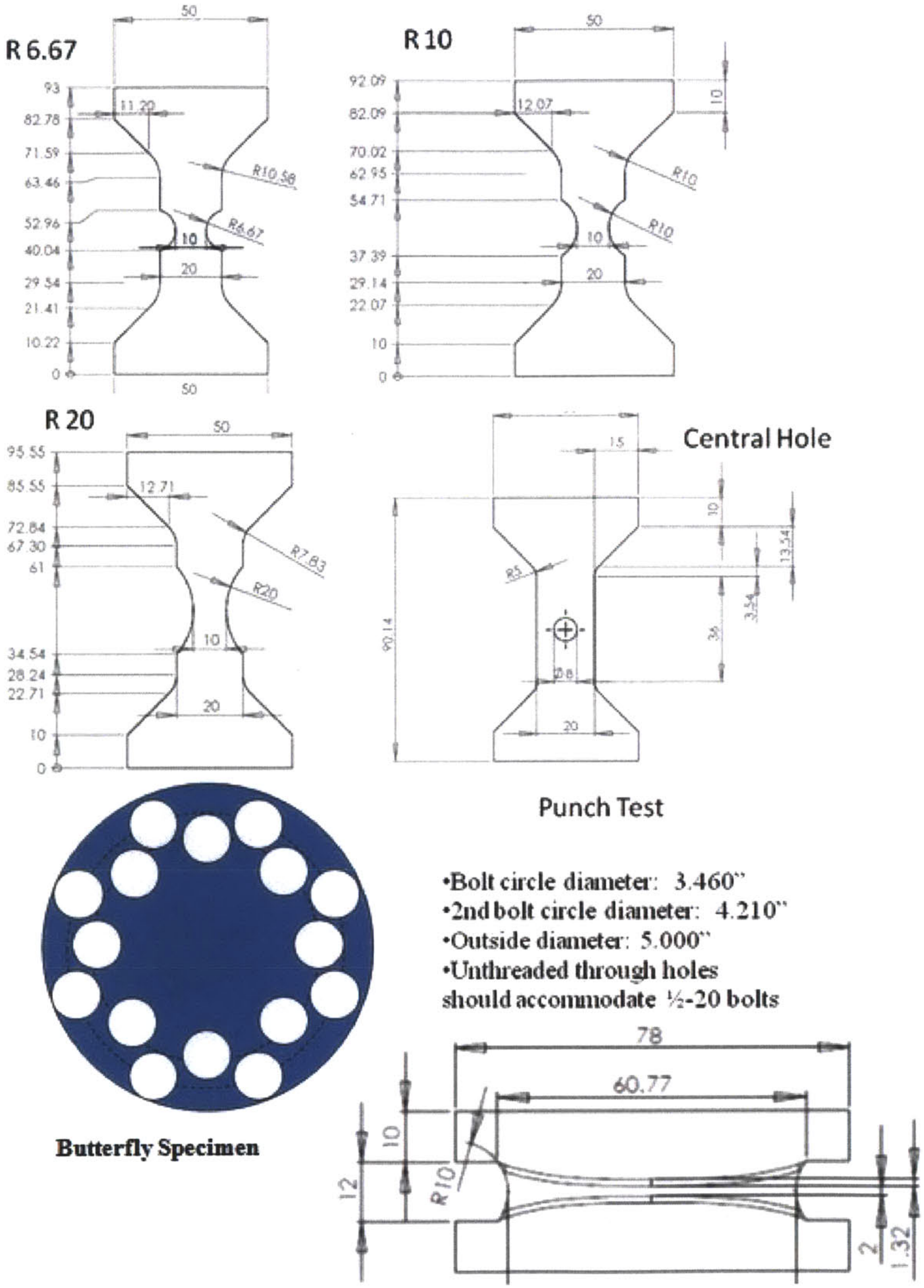

R 6.67

R 10

R 20

Central Hole

Punch Test

•Bolt circle diameter: 3.460"
•2nd bolt circle diameter: 4.210"
•Outside diameter: 5.000"
•Unthreaded through holes
should accommodate ½-20 bolts

Butterfly Specimen

Figure 10 Set of specimens used to calibrate the Modified Mohr Coulomb Criterion

3.1.2 Digital Image Correlation

In this study, numeric simulation is used to determine local stress state and the local strains in the experiments. A comparison between the experiment and the simulation must be done to make sure that the simulation exactly describes the experiment. To do so, Load Displacement curves are compared. It would be too complicated to take into account the mechanical behavior of all the devices that interfere with the displacement measured by the tensile machine. That is why displacement measurements are made on the surface of the specimen itself, using the Digital Image Correlation (DIC), assuming that there is no dependency of the displacement in the depth of the specimen.

Virtual extensometers are used to measure the relative displacement between two points symmetrically opposed to the center of the specimen. The mesh is designed so that its boundaries have the same position as the extensometers extremities. Thus the measured displacement is imposed as the boundary limit in the simulation (Fig. 11). It has previously been verified that the displacement is constant along the width of the specimen at that position.

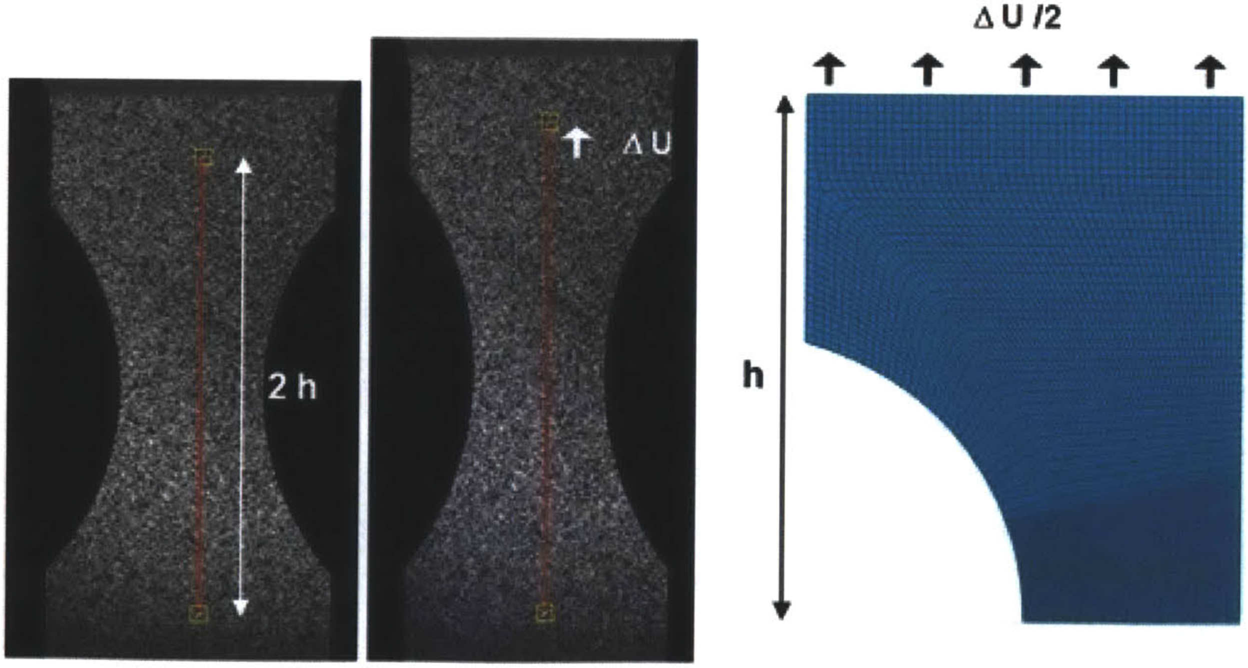

Figure 11 Displacement measured by Digital Image Correlation using extensometer and the corresponding Finite Element Model

The onset of fracture is determined thanks to DIC. The fracture occurs between the last picture where no crack can be seen and the following picture, where a macroscopic discontinuity in the material is observed (Fig. 12). The uncertainty in the exact time when fracture first occurs is exactly the amount of time that separate two successive images. The consequence in the error in displacement is shown in the plasticity validation section.

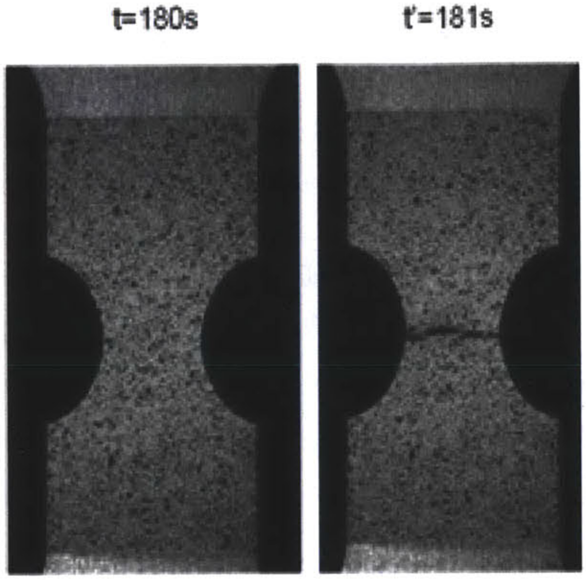

Figure 12 On the left: last picture before the onset of fracture. On the right: first picture after fracture.

3.2 Computational Model

3.2.1 Finite Element Model

Implicit finite element simulations are performed for each experiment using Abaqus/standard. According to Mohr and Dunand (2010), solid elements should be preferred to shell elements. Reduced-integration eightnode 3D solid elements (type C3D8R of the Abaqus element library) are used to mesh the specimens. The mesh size has a very strong impact on the results. A fine mesh is required in the location when localized necking occurs to provide satisfying convergence of the results. That is why a certain type of mesh adapted to the geometry of the specimen is used. The mesh size is dramatically refined in the area of necking. According to the study on the mesh size effect by Mohr and Dunand (2010), a mesh size of 0.1mm per element should be used, providing a good compromise between computation time and accuracy with 0.2% of variation with the result where the mesh size is doubled. The time step is also chosen so that good accuracy is reached. It is also taken advantage in the finite element model of the different symmetries of the problem to decrease the computing time (Fig.13). To be more specific, only one eighth of the specimen is modeled (the upper left quarter of the specimen, with half its thickness), thanks to three planes of symmetry. in the Abaqus code, zero-normal displacement and zero in plane rotation conditions are imposed on the nodes included in each plane of symmetry.

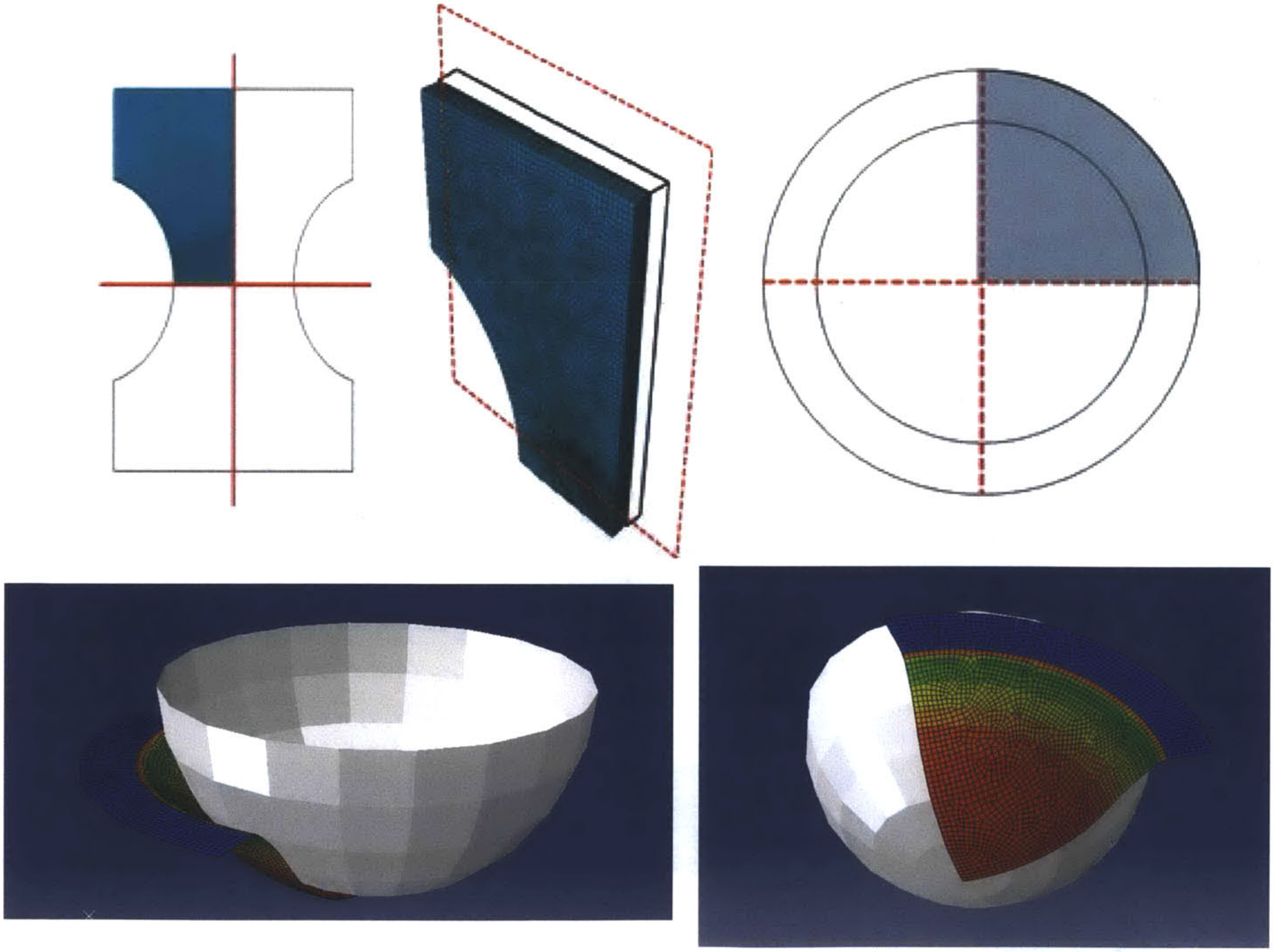

Figure 13 Finite Element meshes of the different specimens, and illustration of the symmetries.

3.2.2 Fracture Locus

Simulations of the experiments are performed to observe the history of triaxiality, Lode angle and strain in the element where fracture first occurs. In order to find out which element corresponds to fracture initiation locus, it is assumed that the fracture location corresponds to the element with the highest equivalent plastic strain.

In the case of the notch specimen, it can be observed from the Finite Element simulation that the point that has the highest equivalent plastic strain at the instant of fracture is right in the middle of the specimen, in terms of thickness, height and width (Fig. 14). It is a little bit different with the central hole specimen, as it seems that the element is not in the border of the hole as expected, but a little bit inside, though it is still in the middle in terms of thickness and height. In the case of the punch test, it is in the middle of the specimen. The strain is rather constant over a wide area in the butterfly specimen.

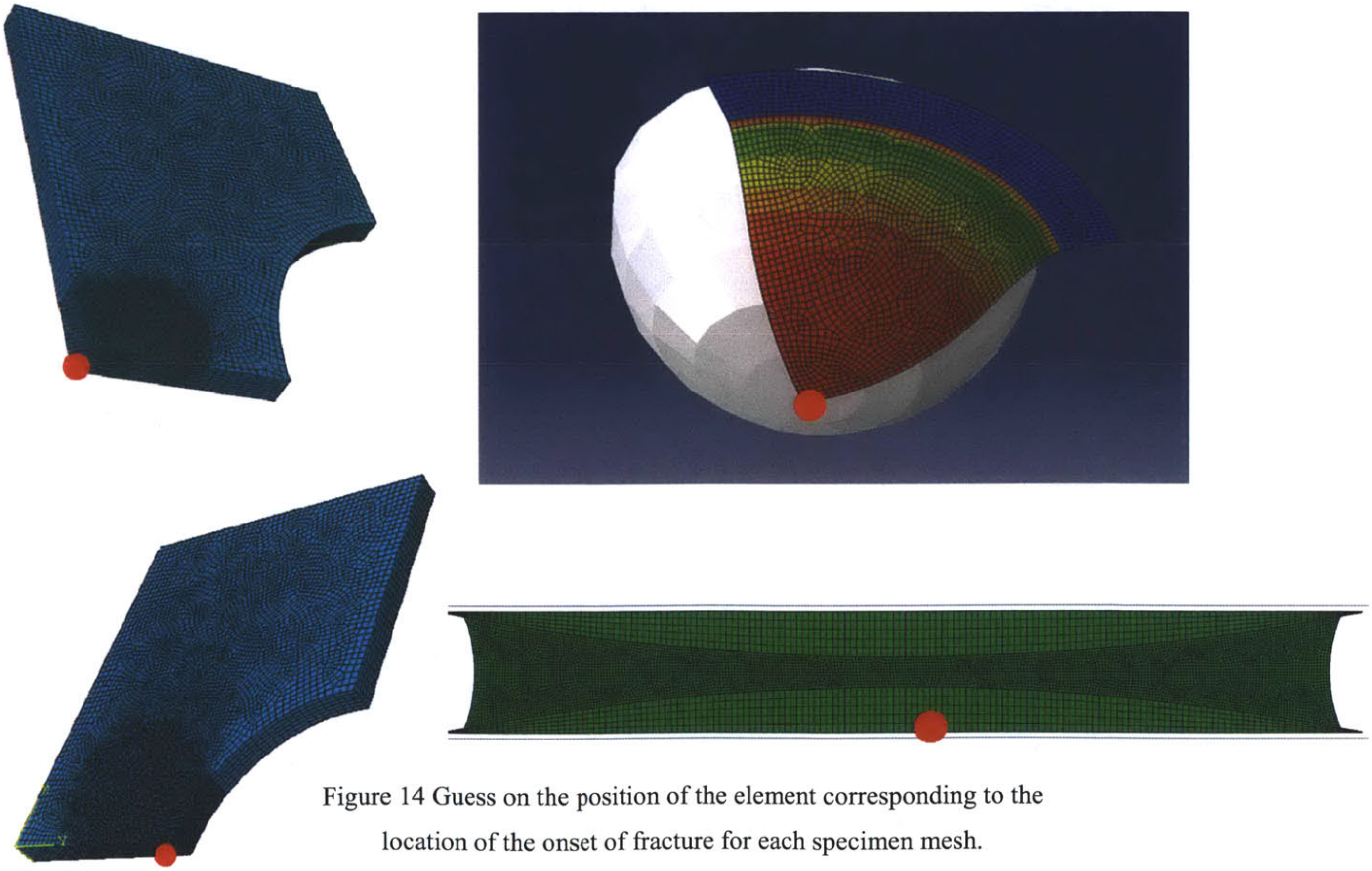

Figure 14 Guess on the position of the element corresponding to the location of the onset of fracture for each specimen mesh.

In order to determine the instant corresponding to the fracture in the simulation, ΔU is defined as the displacement observed with the extensometer and DIC at the moment of the fracture. Triaxiality, equivalent plastic strain and Lode angle at fracture are determined when the displacement in the simulation reaches ΔU (Fig. 15). As ΔU falls between two steps of the simulation, a linear interpolation between the values at the previous step and next step is performed.

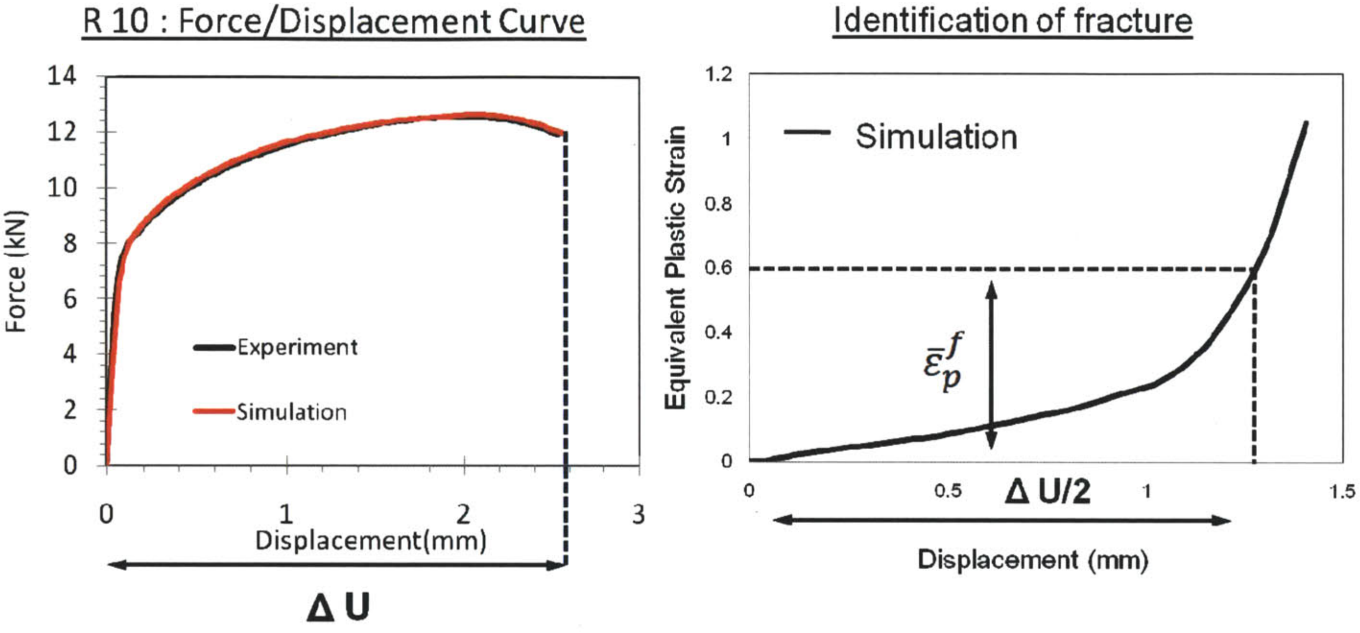

Figure 15 On the left, force versus displacement curve and displacement at fracture. On the right, strain as a function of the displacement and strain at fracture determined by the measured displacement at fracture.

In the case of the punch test, the displacement at fracture in unknown, that is why the reduced thickness of the sheet at the point of fracture t_f is measured to determine the strain and state of stress at fracture in the simulation (Fig. 16).

$$\varepsilon_f = ln\left(\frac{t_f}{t_0}\right) \tag{46}$$

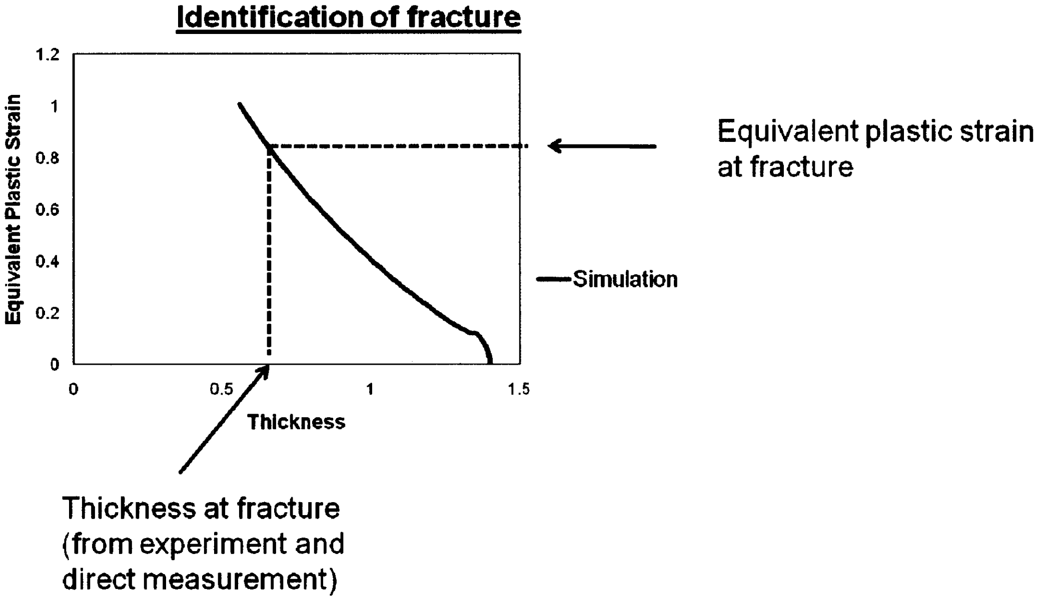

Figure 16 Strain as a function of the thickness in the case of the punch test and strain at fracture determined by the measured thickness at fracture.

3.3 Results

3.3.1 Plasticity Validation

Force-displacement curves obtained by experimental measurements and computer simulation are here compared to decide whether simulation is likely to give a good prediction of the stress state or not. It is assumed that the simulation reaches a good accuracy when the energy corresponding to the gap between the two curves is negligible. It is here visually concluded that the R6.67 notch specimen and butterfly specimen are the only cases where experimental and computational results do not match with satisfaction, as the loading force is overestimated. It must be noted that divergence happens in a range of strains where the maximum load has not yet been reached in the uniaxial test, suggesting that the Hill 1948 model of the behavior of the material itself is responsible for the error, more than an uncertainty in the determination of the hardening law.

In the case of the punch test, DIC has not been performed. This explains why there is not a good prediction of the simulation in terms of load and displacement. Simulation does not take into account the behavior of all the devices located between the specimen itself and the displacement measurement. It confirms the idea that DIC is necessary to determine the displacements in the specimen. On the other hand, a very good level of prediction can be reached if considering the time scale instead of the displacement. It is here supposed to be enough to validate the method.

It can be observed that the uncertainty of the onset of fracture in time leads to an error of 1% in the displacement. However, it corresponds to the point where load falls to zero within the same range of error.

Next two pages: Fig. 17 Comparison of experimental and computer predicted Force displacement curves and fracture locus.

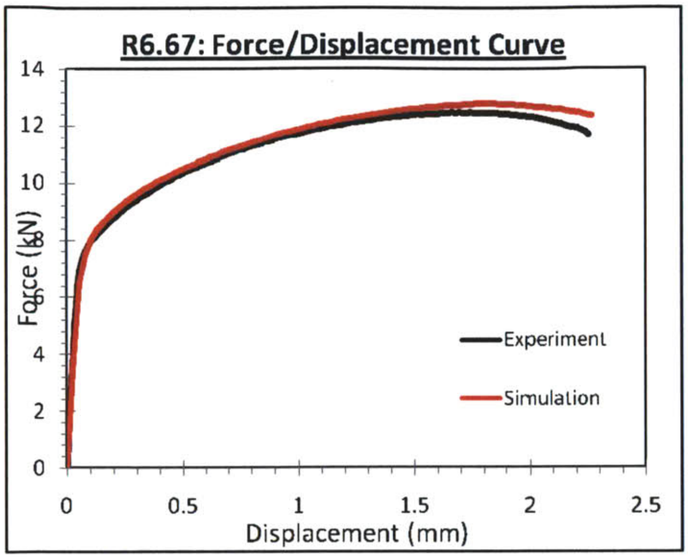
R6.67: Force/Displacement Curve
Force (kN)
0
2
4
6
8
10
12
14
Displacement (mm)
0
0.5
1
1.5
2
2.5
Experiment
Simulation

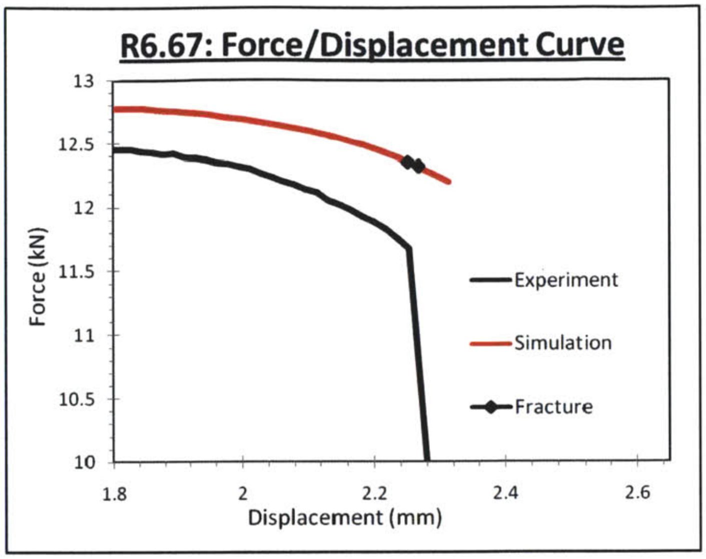
R6.67: Force/Displacement Curve
Force (kN)
10
10.5
11
11.5
12
12.5
13
Displacement (mm)
1.8
2
2.2
2.4
2.6
Experiment
Simulation
Fracture

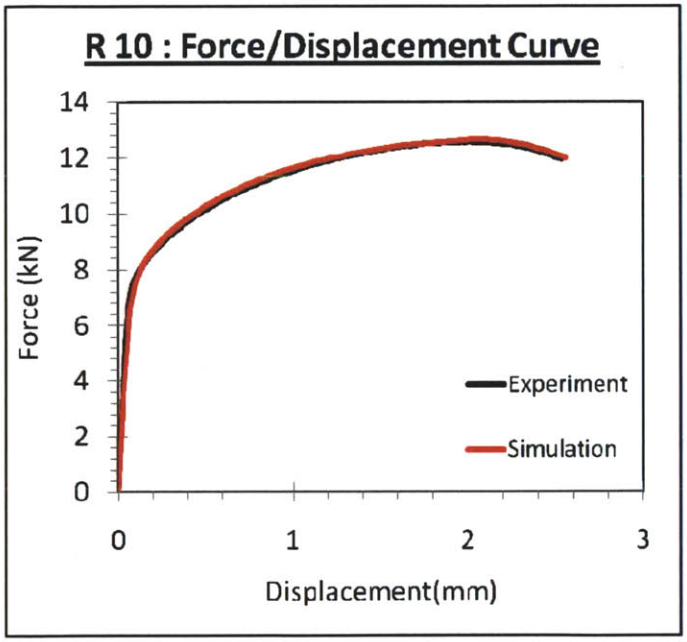
R 10 : Force/Displacement Curve
Force (kN)
0
2
4
6
8
10
12
14
Displacement(mm)
0
1
2
3
Experiment
Simulation

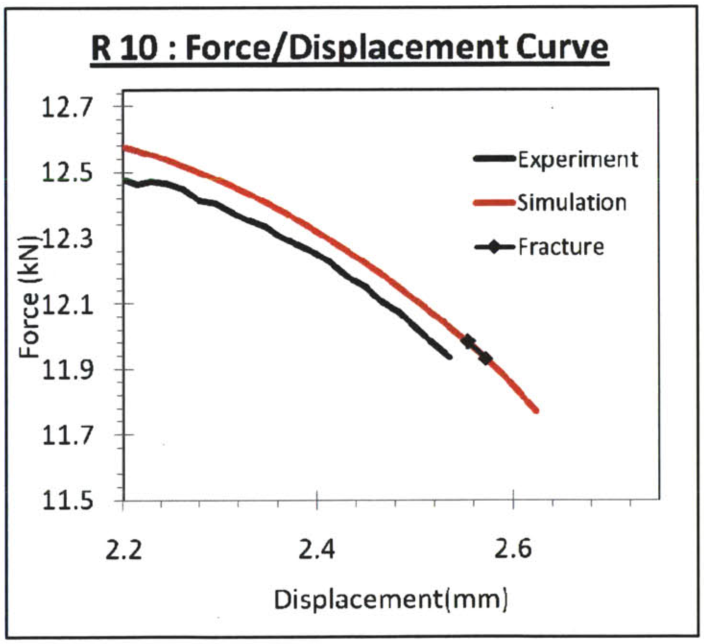
R 10 : Force/Displacement Curve
Force (kN)
11.5
11.7
11.9
12.1
12.3
12.5
12.7
Displacement(mm)
2.2
2.4
2.6
Experiment
Simulation
Fracture

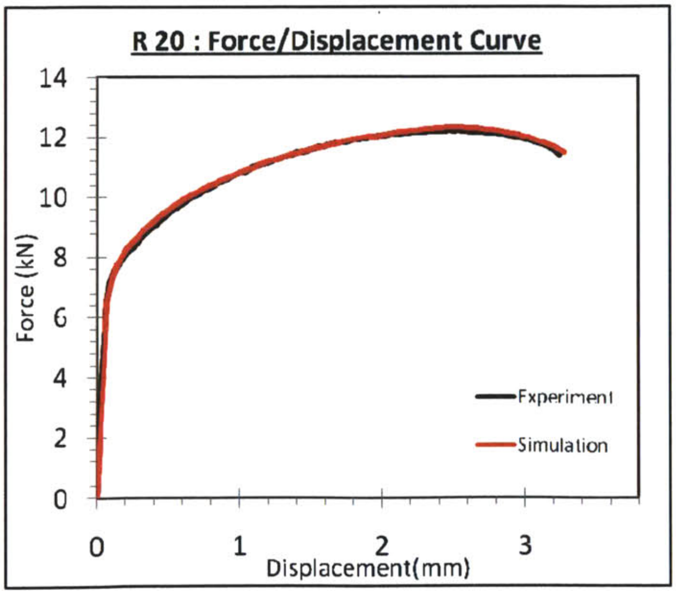
R 20 : Force/Displacement Curve
Force (kN)
0
2
4
6
8
10
12
14
Displacement(mm)
0
1
2
3
Experiment
Simulation

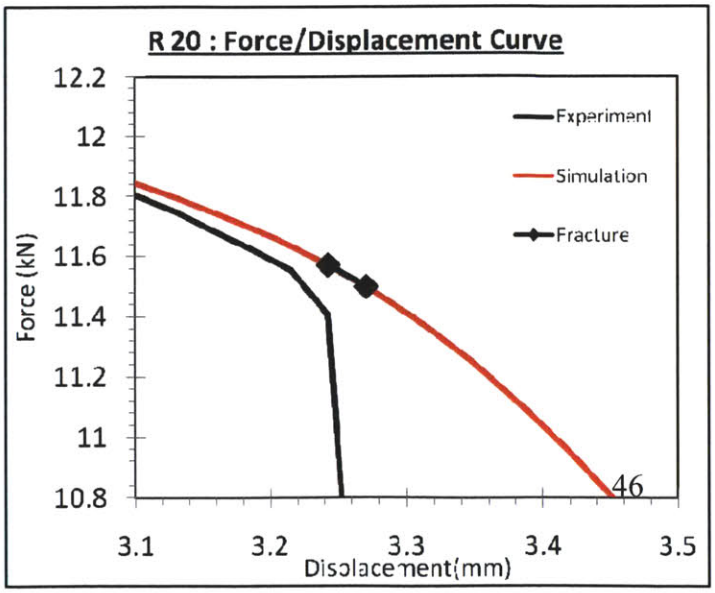
R 20 : Force/Displacement Curve
Force (kN)
10.8
11
11.2
11.4
11.6
11.8
12
12.2
Displacement(mm)
3.1
3.2
3.3
3.4
3.5
Experiment
Simulation
Fracture

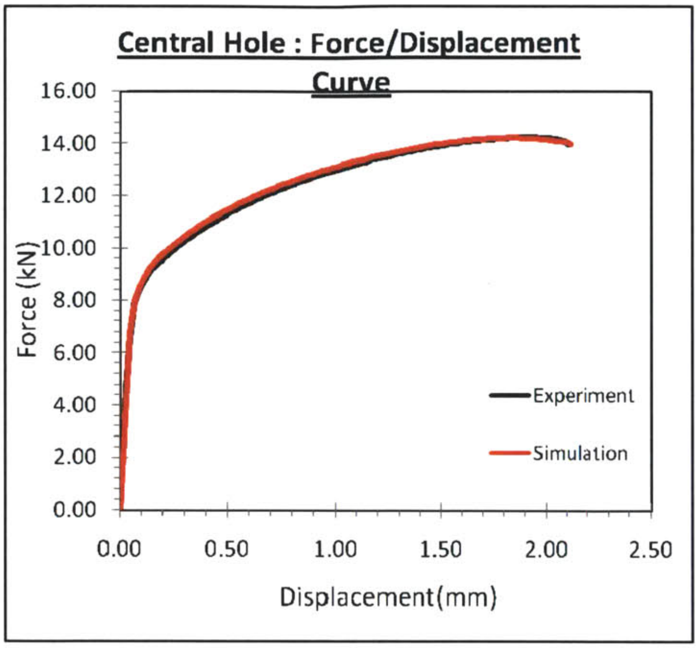

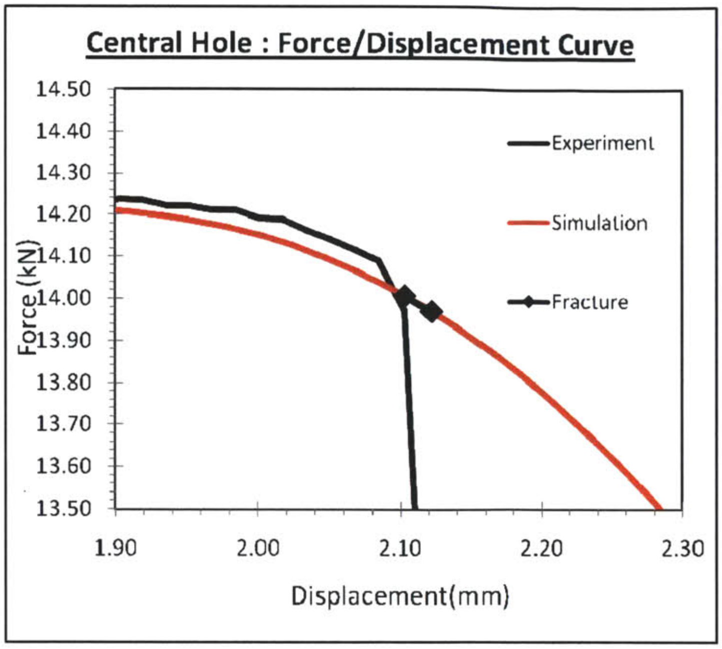

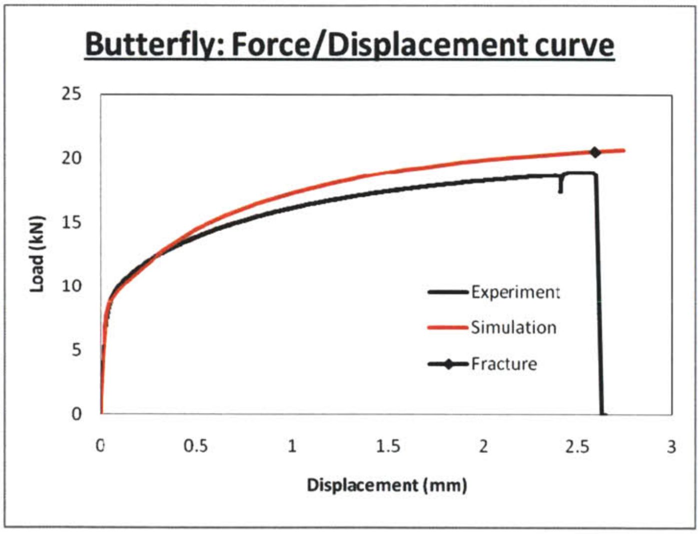

Figure 17 Comparison of experimental and computer predicted Force displacement curves and fracture locus

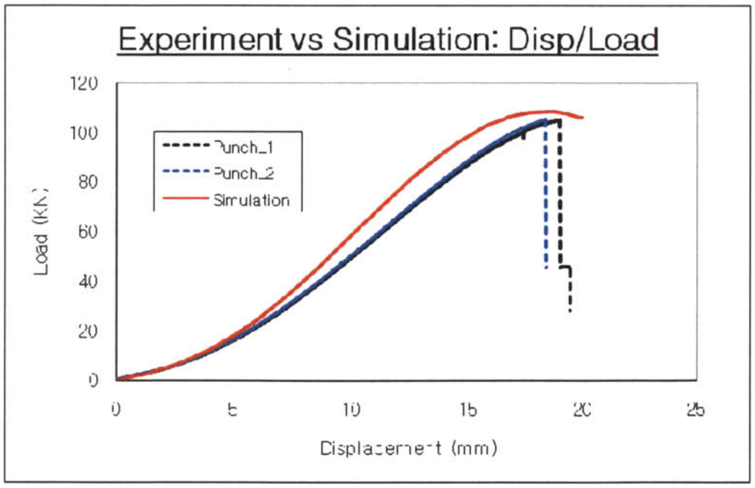

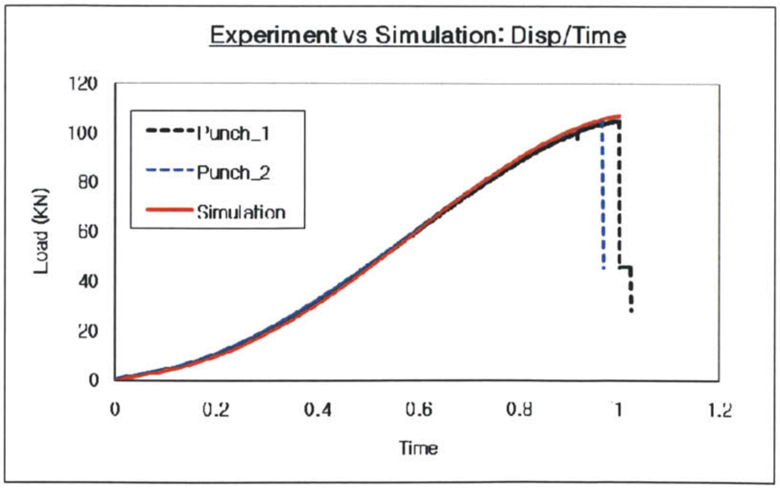

3.3.2 Results

The evolution of the triaxiality and the Lode angle and the values at fracture can now be observed for each specimen (Fig. 18). The uncertainty in time of fracture is shown on the graphs. For a study of experimental and numerical error please refer to Dunand & Mohr (2010).

The stress state varies a lot during the loading for the notched specimens. The stress of state also varies, but in smaller proportions for the central hole specimen, whereas it is constant with the shear test. In the case of the punch test, the variations at the beginning of the loading are more probably due to errors in the computer model. The equivalent plastic strain at fracture is different for each of these tests. It is also true for the different notched specimens, even if the stress state at fracture is almost the same in each case.

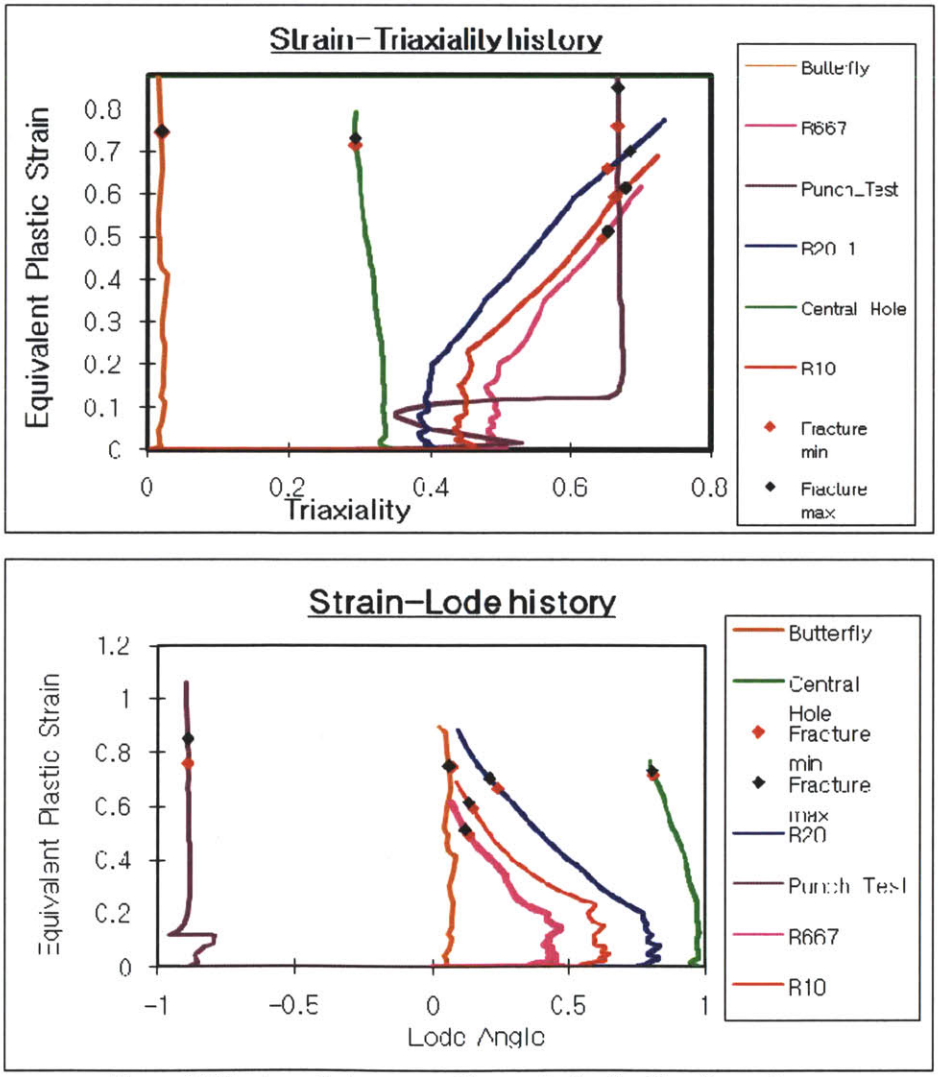

Figure 18 Strain and stress state history during loading for each test.

3.3.3 Identification of the MMC parameters

To determine the three parameters c1, c2, c3 of the Modified Mohr Coulomb criterion that best fits the material, an inverse calibration is done. The method of least squares is used to minimize the distance of the damage at fracture in the simulation to unity for each experiment:

$$[c_1, c_2, c_3] = \arg\min_{c_1, c_2, c_3} \sum_{i=1}^{N} (1 - D^f{}_i(\eta, \bar{\theta}, \bar{\varepsilon}^f))^2 \tag{47}$$

(N is the number of experiments)

A Matlab program using the function fmincon looks for local minima in a space specified by the lower and upper limits for c1, c2, c3. More specifically, the function looks for the closest local minimum to a solution guessed by the user. The method is in fact very unstable, and the results vary a lot depending on the initial value.

To have a good first guess on the parameters, a simpler problem must be considered. That is why the plane stress condition is first assumed to be true. It allows us to solve the equation in a 2D plane instead of a 3D space. In addition, to avoid the inverse problem, it is assumed that the damage function is constant during the loading. If η and θ are constant during the loading, then the equations reduce to:

$$\hat{\varepsilon}^f = f(\eta_f, \bar{\Theta}_f) \quad , \quad \hat{\varepsilon}^f(\eta_f, \bar{\Theta}_f) = 1 \tag{48}$$

The optimization problem reduces to:

$$[c_1, c_2, c_3] = \arg\min_{c_1, c_2, c_3} \sum_{i=1}^{N} (\bar{\varepsilon}_i^f - \hat{\varepsilon}_i^f(\eta, \bar{\theta}))^2 \tag{49}$$

and its solution yields:

$$[c_1, c_2, c_3] = [0.06676, 676.6, 0.9503] \tag{49}$$

Using the above values as initial conditions, the 3D inverse method gives:

$$[c_1, c_2, c_3] = [0.0789, 676.6, 0.937] \tag{50}$$

The results of the calibration are plotted on Fig. 19 & 20.

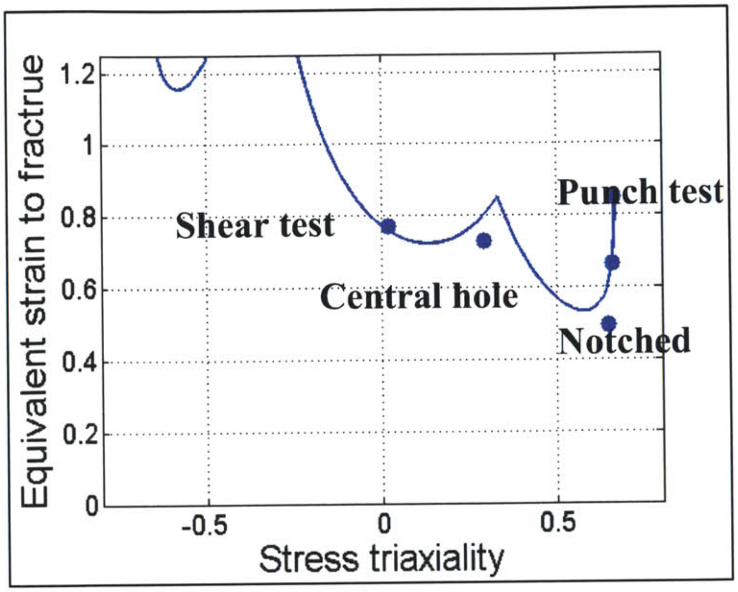

Figure 19 Fracture locus in terms of strain as a function of the triaxiality with the hypothesis of plane strain, and fracture locus of the experiments.

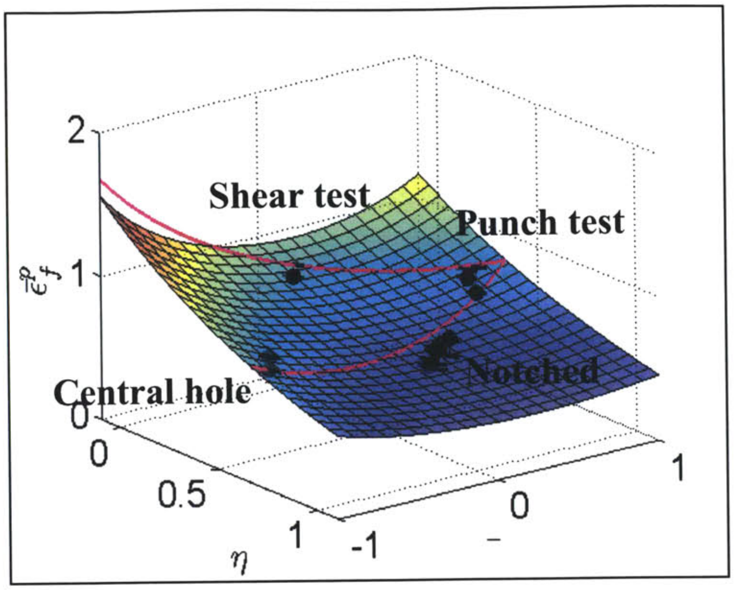

Figure 20 A plot of the full modified Mohr Coulomb criterion. Strain at fracture is a function of Lode angle and triaxiality.

3.3.4 Validation of the model

To compare the prediction of the fracture model to the experiment, the experimental displacement at fracture and the strain are compared to the displacement and strain predicted by the simulation where the damage accumulation reaches 1 (Fig. 21).

$$\Delta U_{\mathrm{num}}(\bar{\varepsilon}^f) =? \, \Delta U^{\mathrm{f}} \tag{51}$$

This is shown in Fig. 21. For each specimen: On the left: damage versus displacement curve with damage and displacement at fracture, and predicted displacement at fracture when damage equals one.

On the right: damage versus strain curve with damage and strain at fracture, and predicted displacement at fracture when damage equals one.

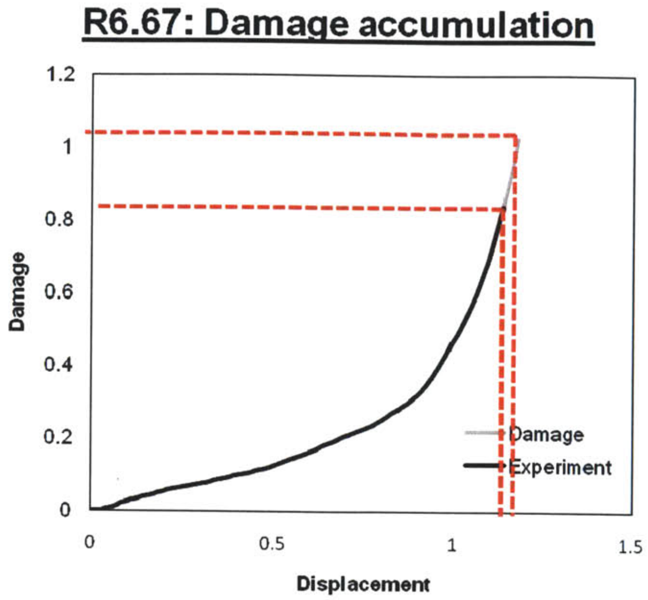
R6.67: Damage accumulation

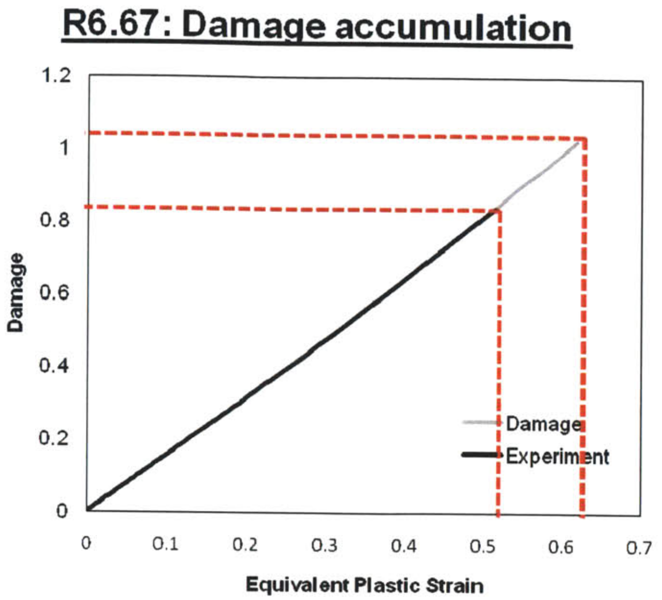
R6.67: Damage accumulation

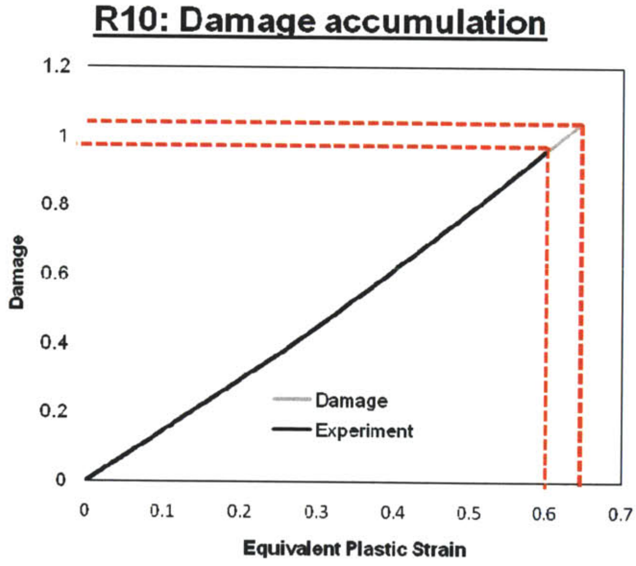
R10: Damage accumulation

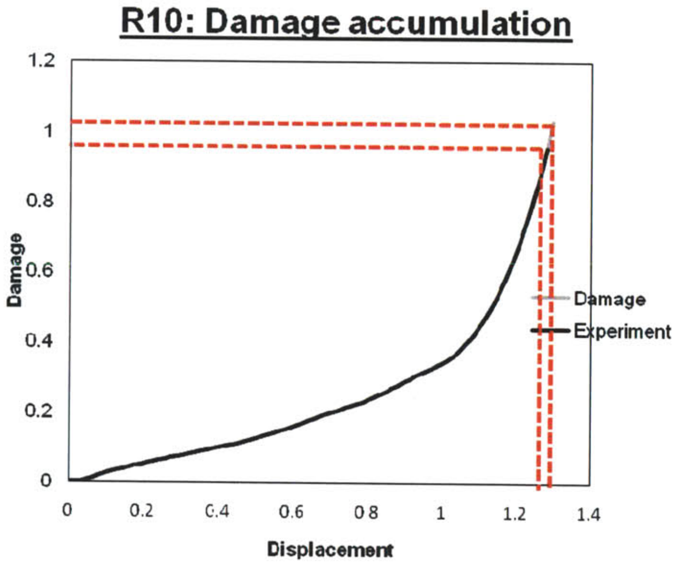
R10: Damage accumulation

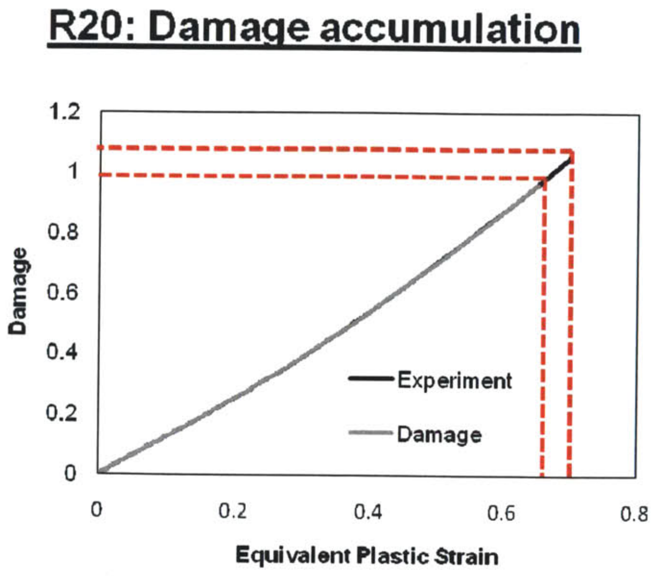
R20: Damage accumulation

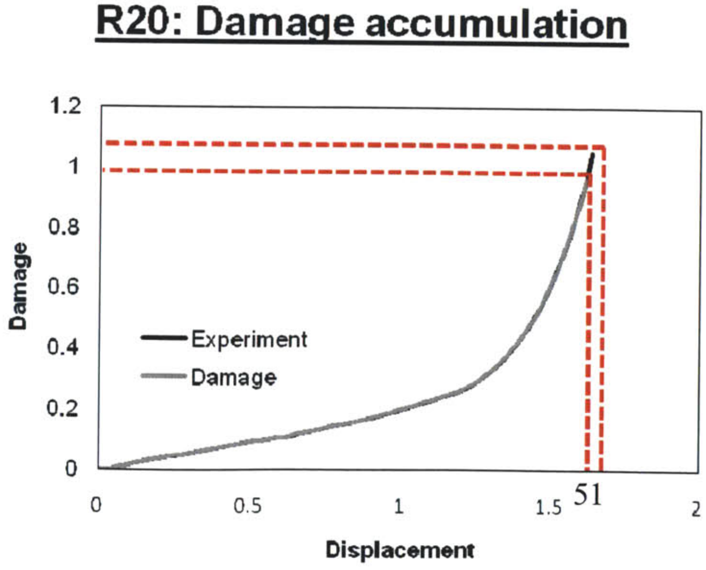
R20: Damage accumulation

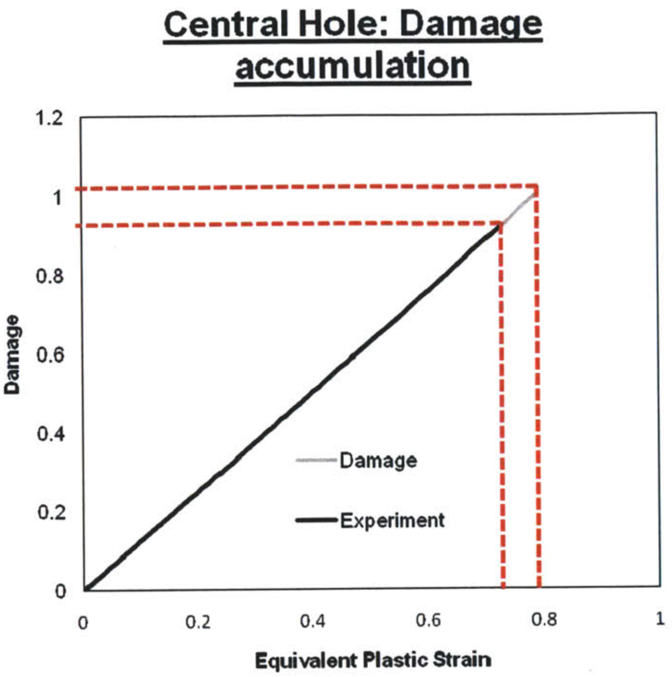
Central Hole: Damage accumulation

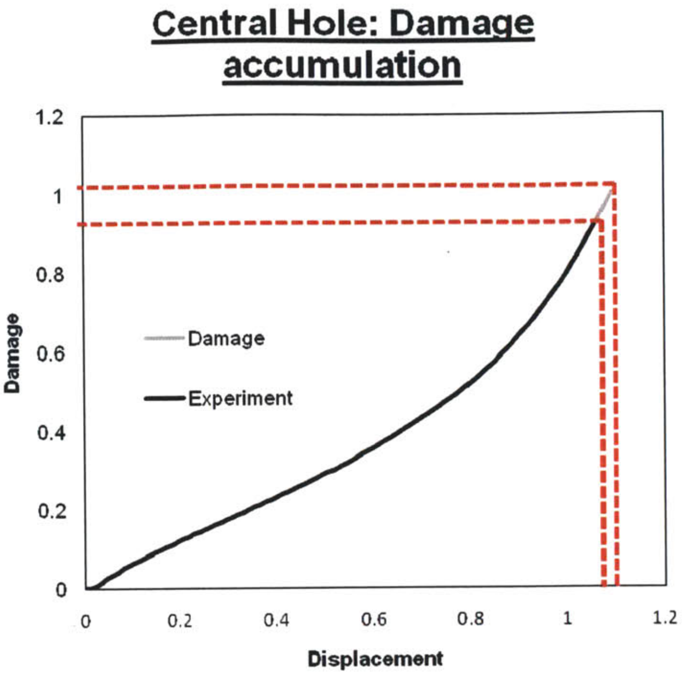
Central Hole: Damage accumulation

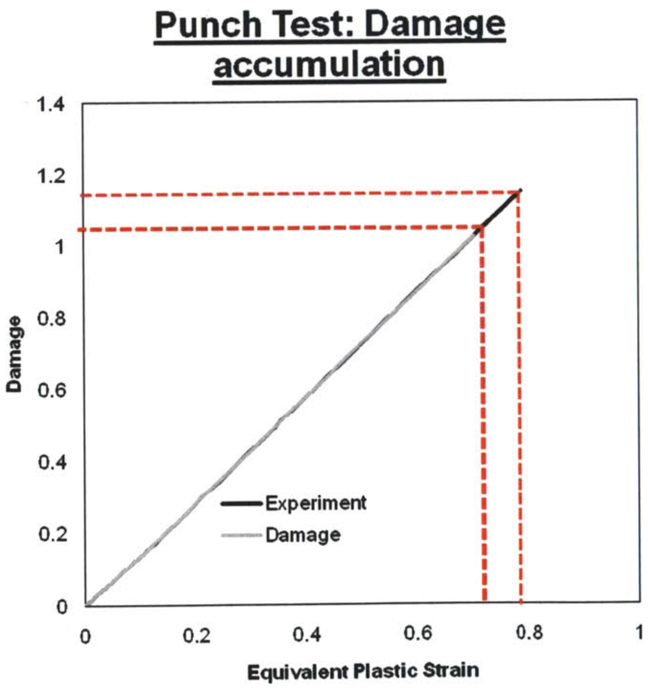
Punch Test: Damage accumulation

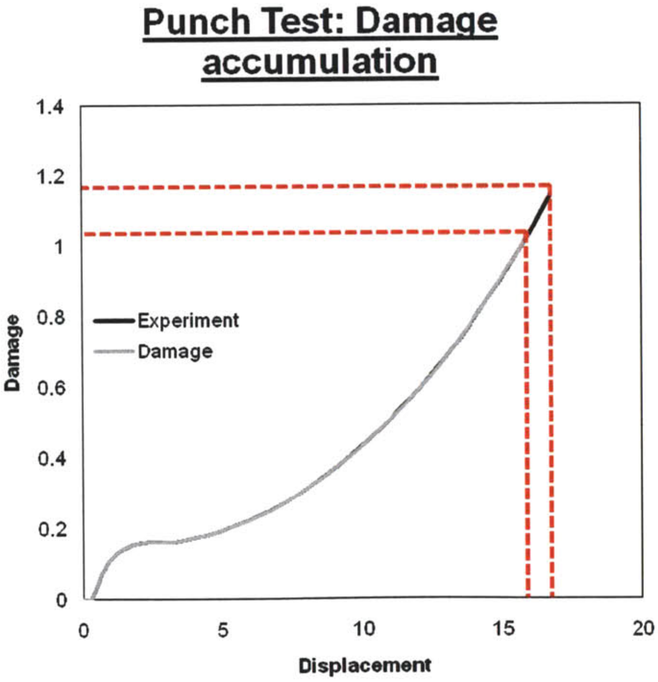
Punch Test: Damage accumulation

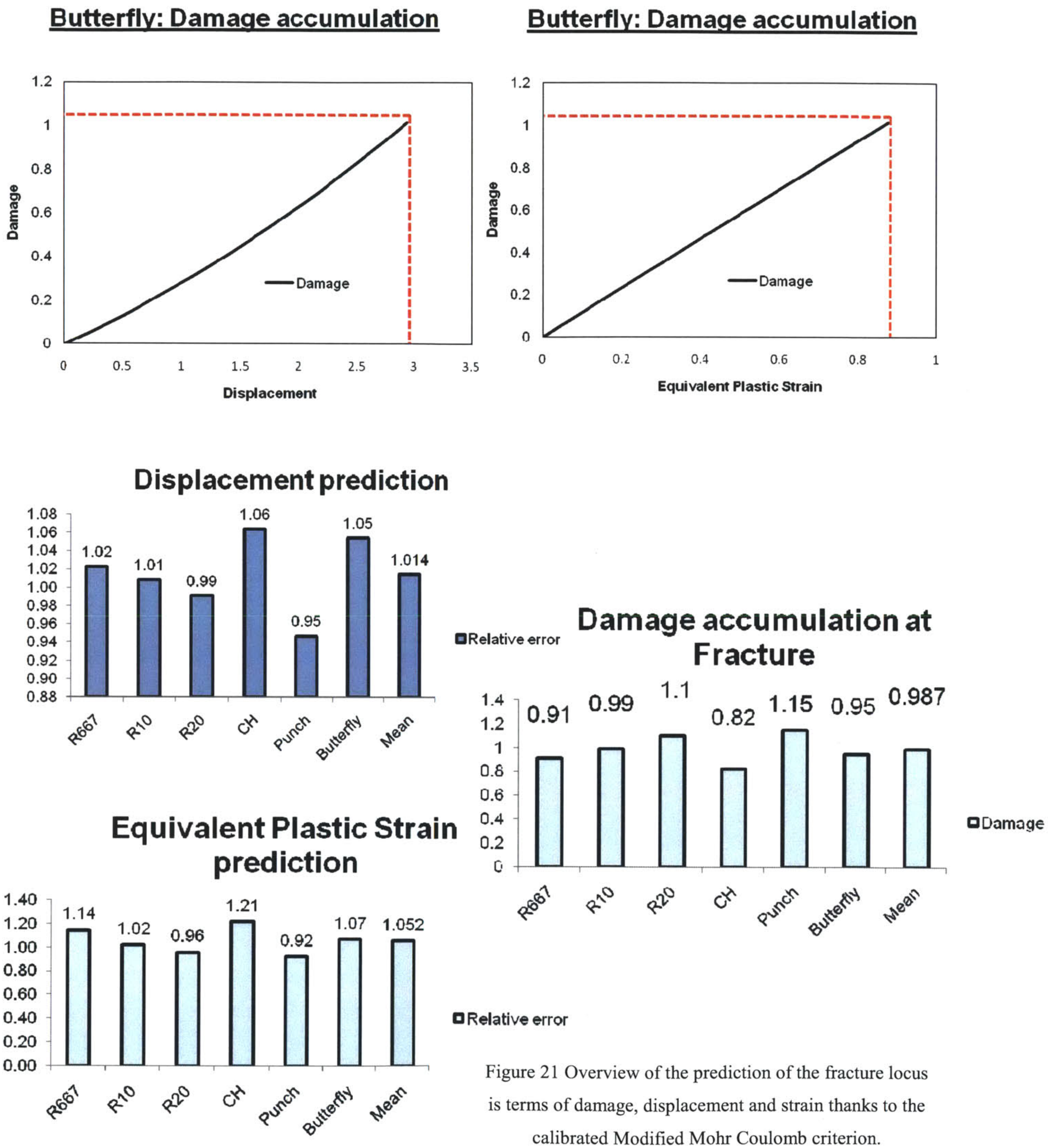

Figure 21 Overview of the prediction of the fracture locus is terms of damage, displacement and strain thanks to the calibrated Modified Mohr Coulomb criterion.

3.4 Conclusion

A method to predict the ductile fracture has been carried out and validated on the example of the Dual Phase steel. A shear test, in addition to the tensile and punch tests, helps to provide better understanding of the effect of triaxiality on the fracture. The observation of the history of triaxiality, Lode angle parameter and equivalent strain show that the trajectories of these quantities at the fracture locus are not linear during the test and change direction as localized necking occurs. This non linear effect is taken into account in the fracture criterion through the use of a damage accumulation function that integrates the plastic strain with a weighted function that depends on the stress state through the triaxiality and Lode angle. The validation of the Modified Mohr Coulomb criterion has shown good accuracy, especially in terms of prediction of the displacement at fracture.

Chapter 4.

IV Effect of reverse loading on Fracture

Experimental procedure

The objective of the experimental part of the research is to enable pre compression of sheet metal by using an Anti Buckling Device and suitable grips for the testing machine, in conjunction with the DIC for strain measurement.

Testing Machine

An Instron tension/shear biaxial testing machine with two independent hydraulic actuators is used. Only uniaxial tests are carried out in the case of this study, therefore the horinzontal actuator is hold in a position where the grips are perfectly aligned.

Traditional wedge grips for uniaxial tension cannot be used as they would open up during the compression phase. Therefore, custom design high pressure grips are used to apply a constant pressure during the whole experiment. These grips can also be aligned precisely in order to delay buckling as much as possible (Fig. 22).

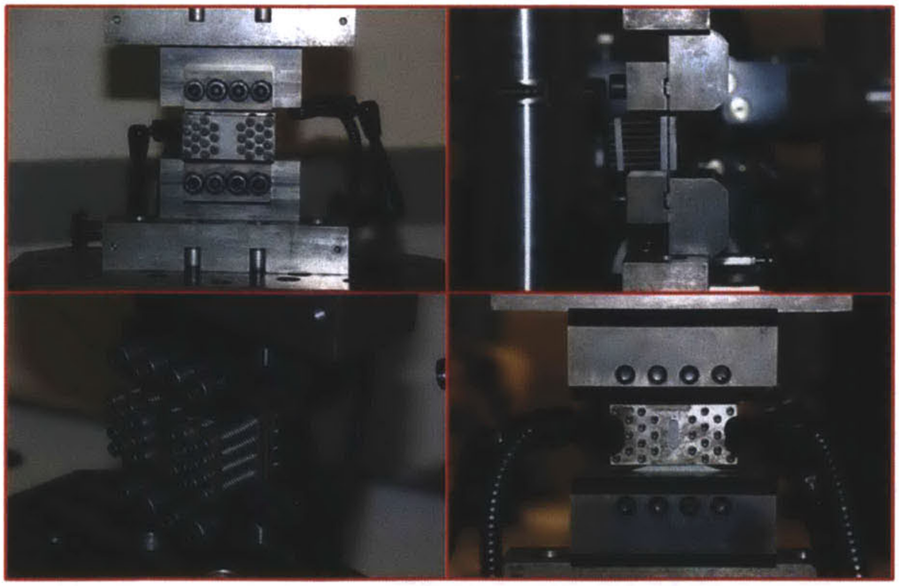

Figure 22 Testing Machine set up

4.1.2 Anti Buckling Device

A device allowing us to apply a relatively high lateral pressure on the specimen, but which remains small compared to the axial stress during the compression phase has been developed by Mansour and Mohr. The specimen has a special shape so that it can be attached to the anti-buckling device (Fig. 23 & 24). The characteristic dimensions of its gage section are the width (w=10mm), height (h=14mm) and thickness (t=1.59 mm). Teflon sheets are inserted between the specimen and the device in order to reduce friction (Fig. 23). A slot has been cut in the front plate of the device to allow the strain measurements by the Digital Image Correlation. Pressure is applied on the specimen by means of some compression springs, so that the thickness of the specimen can increase during the compression phase as an effect of the Poisson's ratio. Compared to Mansour's initial device, the number of springs has been raised to 28 to increase the lateral pressure in order to reach 10% of deformation in compression with a material that has a higher tendency to buckle. The 28 springs are identical; they have an overall length of 32mm, a wire size of 1mm, a outside diameter of 7.1mm, a compressed length of 16.2mm and a rate of 3.1 N.mm-1. The springs are compressed to 17mm. The total force applied by the springs reaches approximately 1300N at the beginning of the test. It remains almost constant until buckling occurs as the variations in compressed length of the springs remains small compared to the initial compressed length. The force corresponds to a pressure of 3 MPa, which is very small in comparison with the stresses applied in the loading direction. Therefore, we consider that this contribution can be neglected.

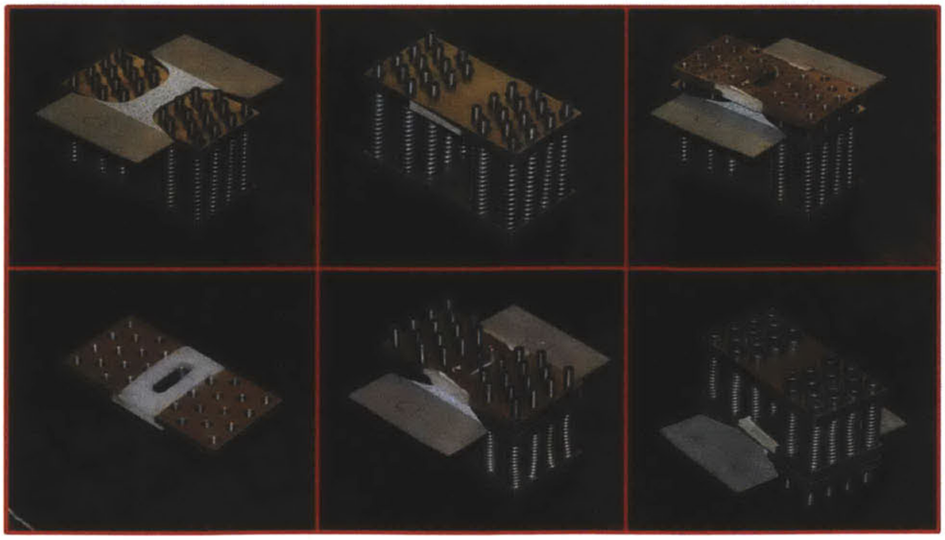

Figure 23 Procedure to install the Anti Buckling Device

4.1.3 Specimen

The design of the specimen had to fulfill two different requirements. The fracture of the material is observed in tension, therefore the specimen has to possess the features of a tensile specimen. It is important to maintain a relatively uniform stress and strain field through the gage section, which requires to design the specimen in order to obtain a large length to width ratio. These sheet metal specimens are submitted to an in plane pre compression, during which buckling must be avoided. A low length to width ratio allows delay the buckling during compression. A compromise is found in the design of the specimen (Fig. 24).

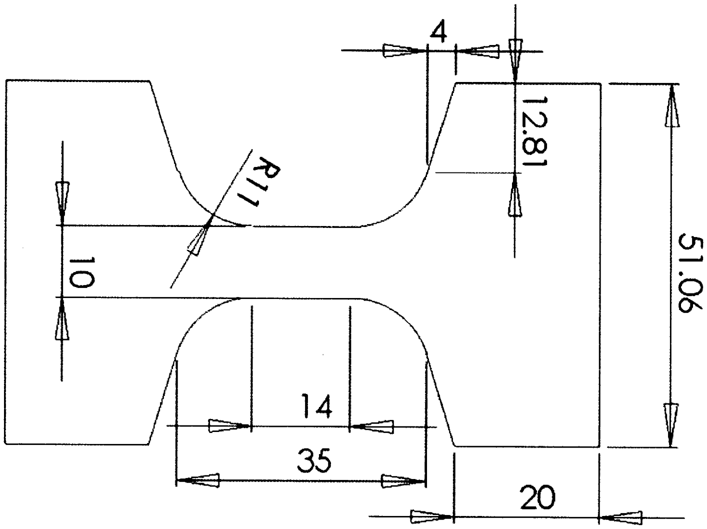

Figure 24 Compression Tension Specimen Geometry

4.1.4 Digital Image Correlation

Displacements are measured by means of the Digital Image Correlation (DIC) method. It consists in observing with a video camera the evolution of the surface of the specimen, considering that these displacements remain homogeneous through the thickness. The specimen is painted in white and then sprayed with a black speckle pattern. The VIC-2D software, which is a Digital Image Correlation (DIC) package made by Correlated Solutions, Inc (West Columbia, SC), is able to track the displacement of arbitrary positions in each of the pictures by comparing the deformed image to the original. Vertical displacements are measured by comparing the evolution of the relative positions of two points initially placed on a vertical line. In the case of our experiments, it can only be done in the area corresponding to the slot made in the front plate.

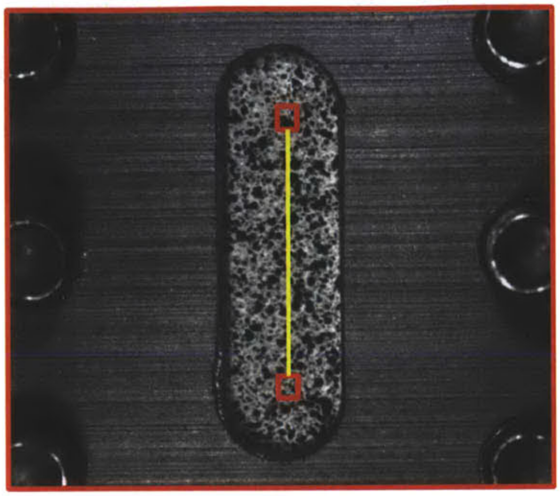

Figure 25 Digital Image Correlation with extensometer through the window of the anti buckling device

4.1.5 Procedure

The specimen have been extracted from sheet metal in the 0 degree rolling direction using an abrasive cutting machine (OMAX waterjet). In order to perform DIC measurement, the specimen are cleaned with acetone, and then painted in white and black paint is then carefully spread in order to get a black speckle pattern. Teflon sheets are placed between each face of the specimen and the device. Teflon is removed in the slot area. The specimen is then carefully placed in the anti-buckling device, so that they are centered. The painted side has to face the plate with the slot. Screws are tightened so that the two plates that compress the springs are parallel and at a distance of 17mm from each other. It guaranties that the springs are all compressed equally. The specimen is then placed in the grips.

4.1.6 Experimental results

A tensile test was first performed all the way to fracture to determine the ductile fracture in tension in the absence of any reverse loading. Such a test has then been repeated with the anti-buckling device to validate the assumption that the device does not have any impact on the plasticity and fracture behavior of the specimen. Stress Strain curve and fracture locus are compared.

Then, a compression test using the anti buckling device is performed. The purpose of is to determinate when buckling first occurs and make sure that it allows us to perform reverse loading tests in the range of strains that we are interested in. At 15% true strain, buckling had not yet occurred and the test was completed. When the device was removed after the experiment, an effect of barreling could be observed on the deformed specimen. Such a test also makes it possible to predict the corresponding displacement that has to be applied when driving the Instron Machine in order to reach a chosen deformation in compression for reverse loading tests. It was decided to observe the ductile fracture in the case of a reverse loading for a pre compression of 2.5%, 5%, and 10% of strain. A constant speed for the crosshead is used to first apply a suitable displacement in compression to reach the desired strain. Then, the crosshead move back at the same speed and applies tension to the specimen up to fracture.

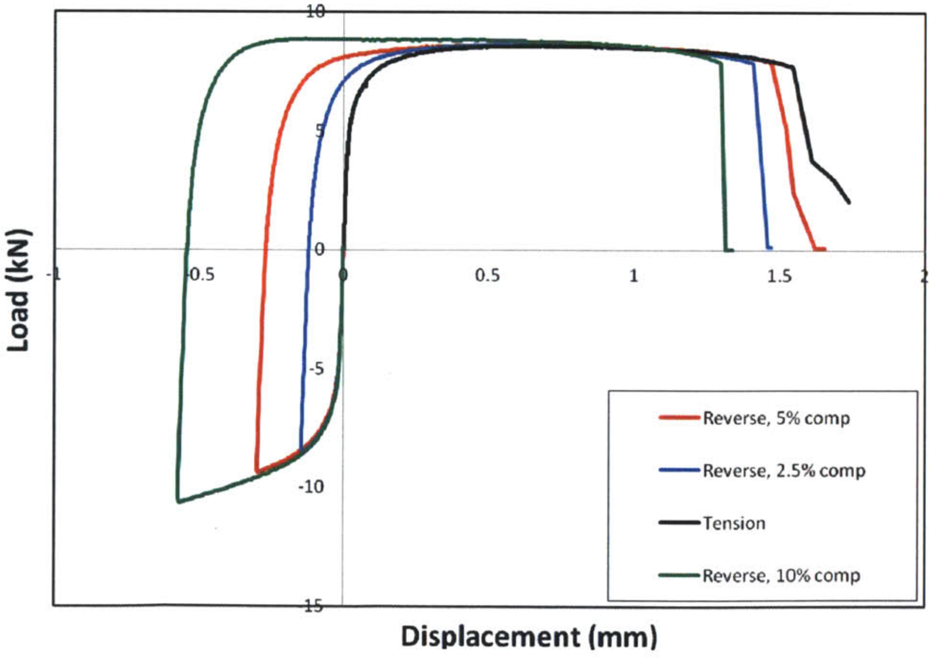

Figure 26 Load Displacement obtained for reverse compression tension uniaxial tests

Finite Element Model

The optimization method compares the load displacement curve of the simulation and the experiment for all levels of pre compression. Therefore, the Finite Element model has to be solved four times at each step of the optimization procedure, and many steps are necessary to find a solution. As a consequence, this strong computation time constraint leads to the use of a computationally efficient Finite Element model.

Each experiment is simulated using an Implicit Finite Element software (Abaqus/Standard). In order to save some computation time, some simplifications are used. It is assumed that there are three planes of symmetry for the problem. Therefore, only the upper left part of the specimen with half thickness is meshed. If this is true in the experiment at the initial state only, this is enforced to remain true in the Finite Element model at all times. In order to capture the localized necking effect in the thickness of the sheet material, five reduced integration eight node 3D solid elements of type C3D8R are incorporated in the mesh along the thickness. The mesh is highly biased to concentrate computation power on the gage section that undergoes high deformations (Fig. 27). The numerical specimen is designed so that a virtual extensometer matches the length of the extensometer used in the Digital Image Correlation method. Force versus virtual extensometer displacement curve is extracted from each simulation.

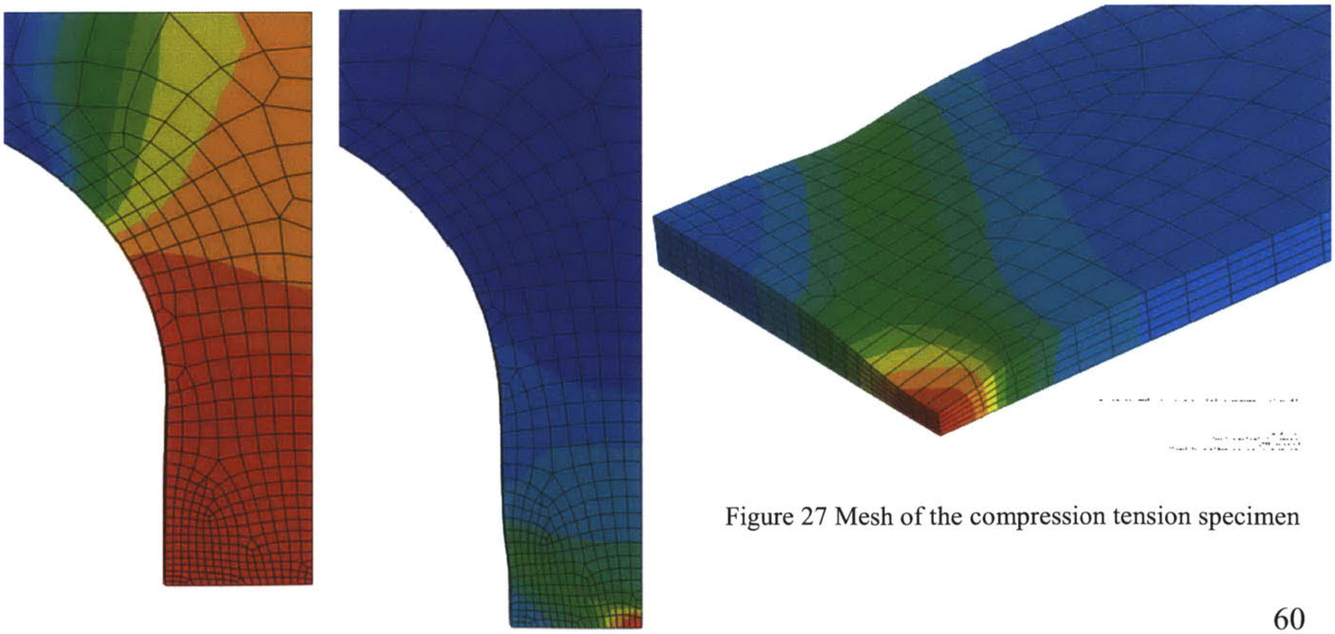

Figure 27 Mesh of the compression tension specimen

4.3 Results

4.3.1 Plasticity Validation

The optimization method has been performed and gives a set of parameters for the modified Yoshida plasticity model shown in Table 5.

Non Linear Kinematic		Linear Kinematic	Isotropic	
C (MPa)	γ	H (MPa)	Q (MPa)	b
3800	15.5	0.0011	341	232

Table 5 Numerical values for the optimized parameters of the modified Yoshida plasticity model

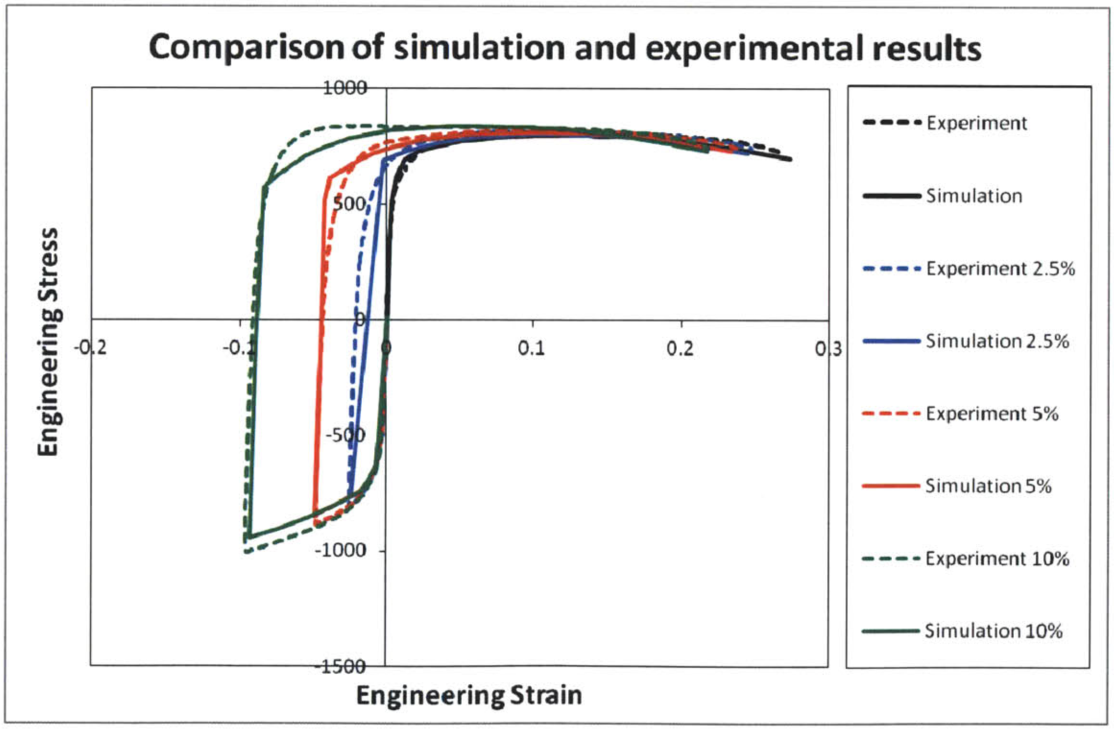

Figure 28 Overview of the computer prediction of the load displacement for each compression tension test with the optimized modified Yoshida plasticity Model

For each level of compressive pre strain, a Finite Element simulation was run with the optimized set of parameters for the modified Yoshida plasticity model. For each test, the load displacement curves are compared (Fig. 29). It is observed that the prediction of maximum load and load after diffused necking and localized necking is accurately predicted by the model. However, the model fails to reproduce the transition between the elastic and the plastic phase with sufficient accuracy. More advanced models could be used to address this issue, but it is assumed here that it would have limited effect on the prediction of the stress and strain state in the gage section at very large tensile deformation.

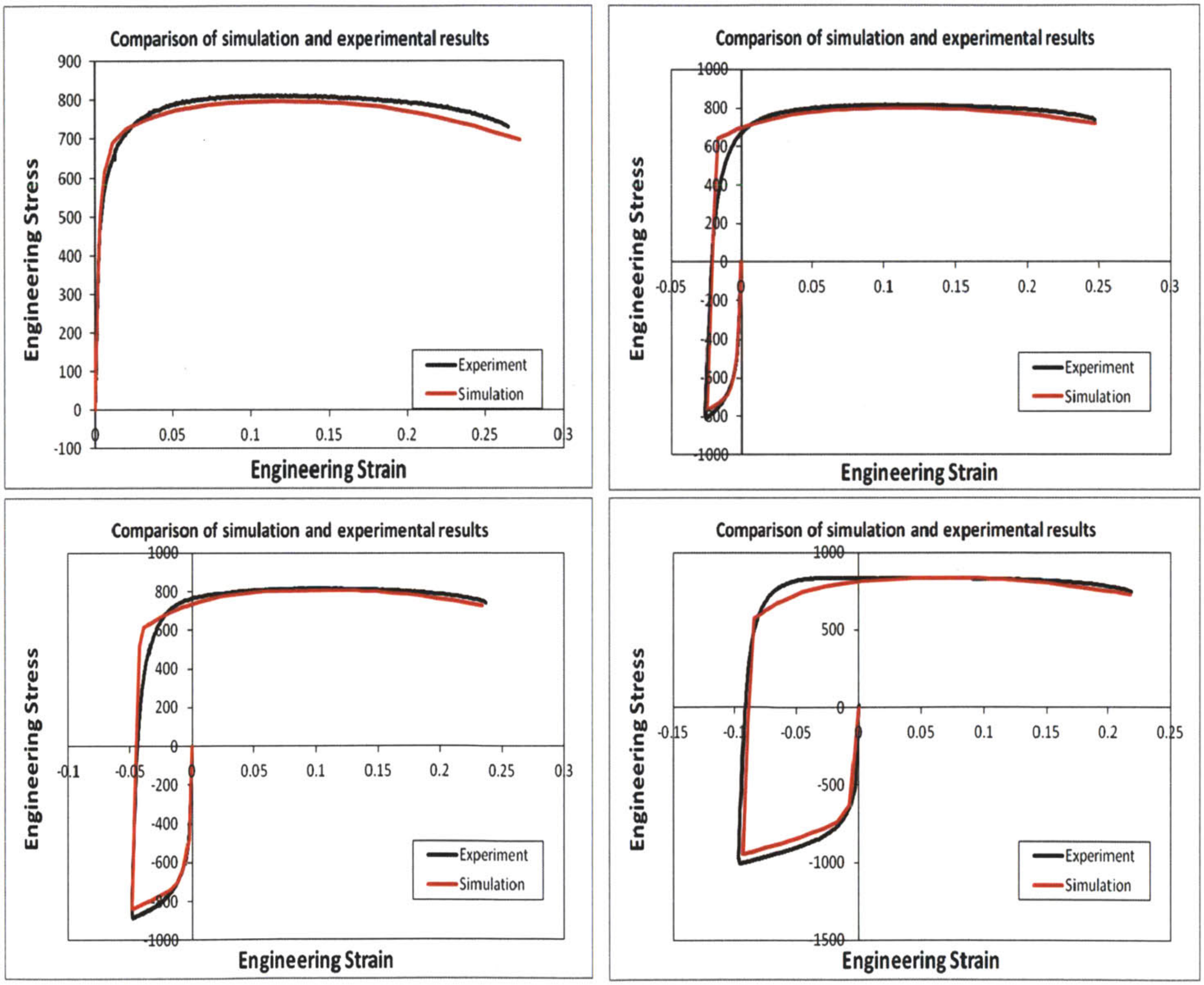

Figure 29 Prediction of the load displacement for each test

4.3.2 Evolution of Stress and Strain States

The history of local stress and strain state has been predicted in the material during the entire test for each experiment using computer simulation. The evolution of the strain and stress state is observed in the space of triaxiality, Lode angle parameter and equivalent plastic strain (Fig. 31 & 32). The loading path in this space has been plotted at the fracture locus (Fig. 30). It is difficult to determine experimentally where the crack initiates, therefore it will be here assumed than the node with highest plastic strain at fracture corresponds to the locus of the onset of fracture.

The stress triaxiality η is proportional to the ratio of the first invariant of the Cauchy stress tensor, I_1, and the second invariant of the deviatoric stress tensor, J_2,

$$\eta = \frac{\sigma_m}{\bar{\sigma}_{VM}} \qquad \text{with} \quad \sigma_m = \frac{tr[\underline{\underline{\boldsymbol{\sigma}}}]}{3} = \frac{I_1}{3} \quad \text{and} \quad \bar{\sigma}_{VM} = \sqrt{3J_2} = \sqrt{\tfrac{3}{2}\underline{\underline{\mathbf{s}}} : \underline{\underline{\mathbf{s}}}} \qquad (52)$$

where $\underline{\underline{\mathbf{s}}}$ is the deviatoric stress tensor. The dimensionless Lode angle parameter, $\bar{\theta}$, depends on the ratio of the second and third invariants of the deviatoric stress tensor, J_2 and J_3. Its definition reads

$$\bar{\theta} = 1 - \frac{2}{\pi}\arccos\left[\frac{3\sqrt{3}}{2}\frac{J_3}{\sqrt{J_2^3}}\right] \quad \text{with} \quad J_3 := \det[\underline{\underline{\mathbf{s}}}]. \qquad (53)$$

The triaxiality and Lode angle parameter have a constant negative value during the compression phase. Then they take the corresponding positive constant value as the loading is reversed to tension. After the onset of diffused necking, the values of both these stress invariant change progressively, as the stress state becomes biaxial with necking.

Furthermore, the equivalent plastic strain at fracture increases with the pre-compression maximum strain. However, it seems that the pre compression phase has a limited effect on the values of triaxiality and Lode angle parameter at fracture.

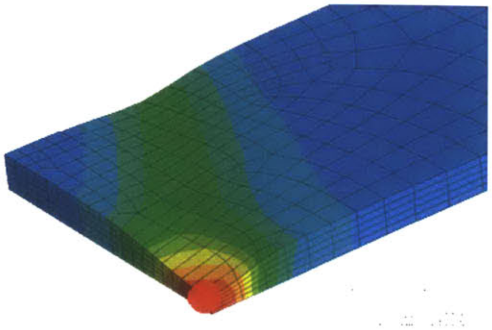

Figure 30 Color coded plot of the equivalent strain in the Dogbone specimen at fracture

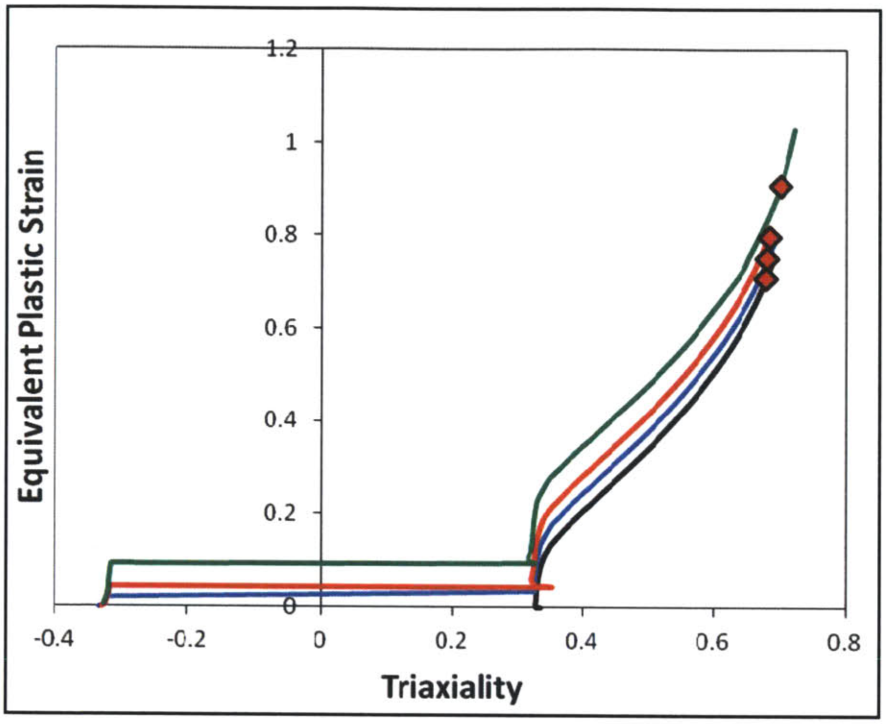

Figure 31 History of the loading path in the space of triaxiality and equivalent plastic strain for all levels of pre strain

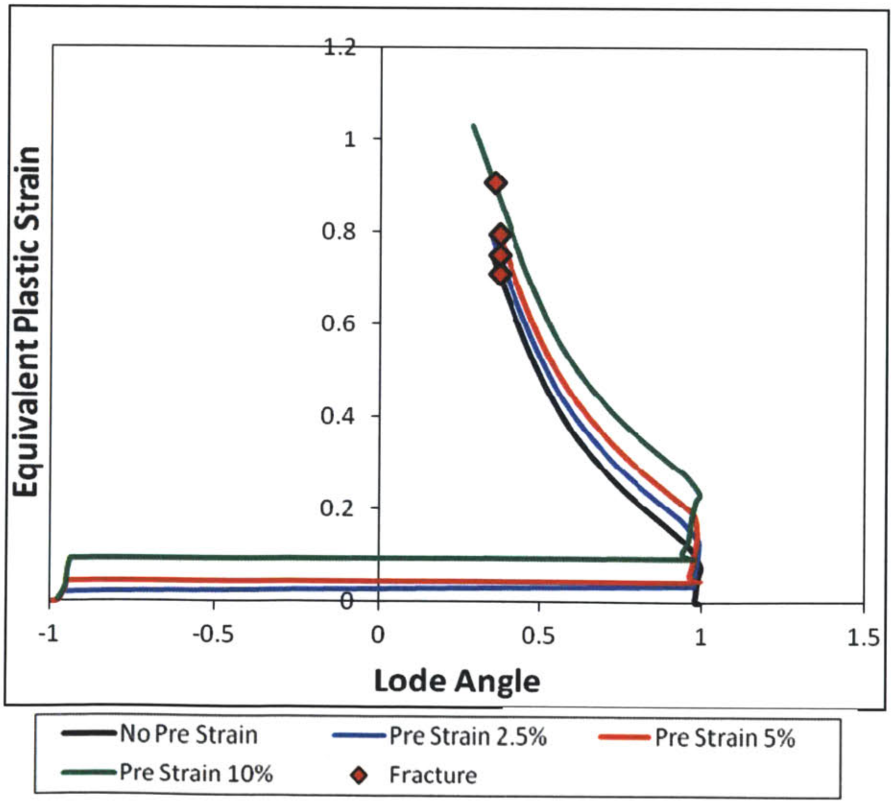

Figure 32 History of the loading path in the space of Lode angle parameter and equivalent plastic strain for all levels of pre strain

4.3.3 Damage accumulation

The curve of the evolution of plastic strain with triaxiality can be translated by substracting the amount of plastic strain that has been accumulated during the compression phase and the tension phase necessary to come back to a global displacement corresponding to the initial state. In these conditions, the material obtained after coming back to zero displacement can be considered as a new material. It is observed that this transformation of the material has little effect on the equivalent plastic strain at fracture (Fig. 33).

In the frame of the theory of damage accumulation, it can be concluded that little damage has been accumulated during the compression phase, causing the fracture to occur at a similar moment in the plastic strain – triaxiality – lode angle space.

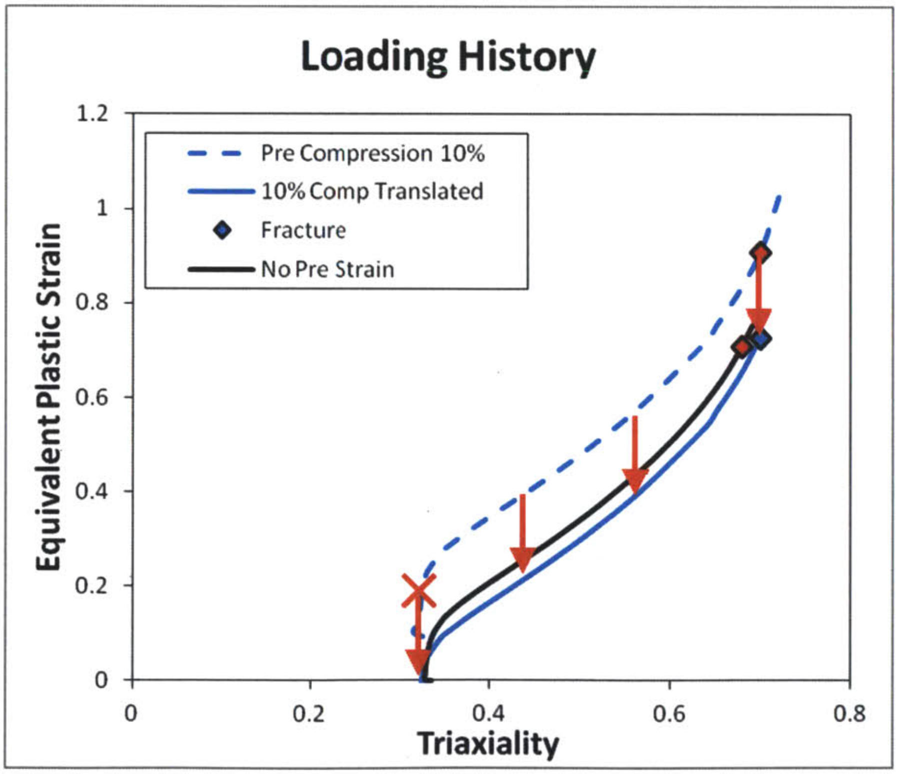

Figure 33 History of loading path and fracture in the space of triaxiality and equivalent plastic strain considering the return to zero displacement as a new initial state

A simple damage accumulation model is here introduced to better understand the implications of the results of this study.

The damage function is defined as:

$$D\left(\bar{\varepsilon}^{p}\right)=\int_{0}^{\bar{\varepsilon}^{p}} \frac{d\varepsilon}{\hat{\varepsilon}_{f}(\eta)} \tag{54}$$

with:

$$D\left(\bar{\varepsilon}^{f}\right)=1 \tag{55}$$

when the damage function reaches unity, Fracture occurs.

It is particularly interesting for this study to observe the dependency of the weighting function on the triaxiality. In the range of negative triaxialities, corresponding to the compression case, it can be observed that these models predict dramatically increased values of the function (Fig. 34). This means that very little damage is accumulated when integrating during the compression phase.

The results of the study validate such a prediction of low damage accumulation by these phenomenological models.

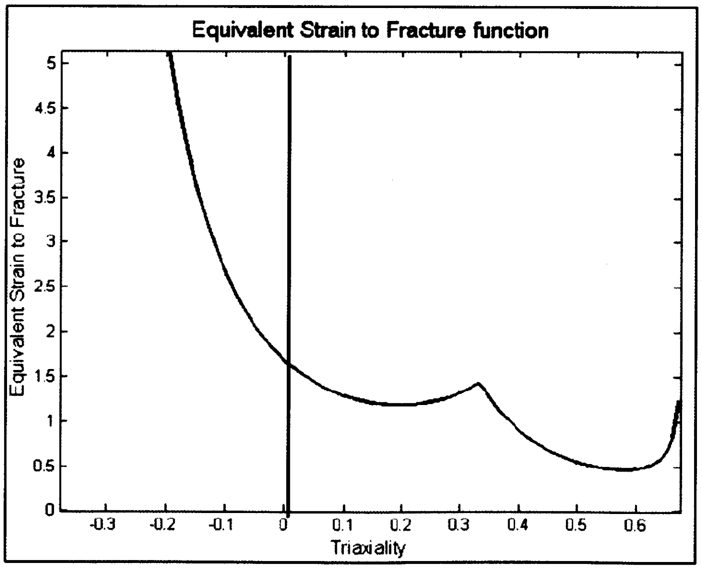

Figure 34 Dependance of the weight function of the damage accumulation model on the triaxiality

4.3.4 Modified Mohr Coulomb Criterion

As an illustration of the prediction of a phenomenological model for fracture, the Modified Mohr Coulomb criterion was used. The parameters for this material have been calibrated in Carey Walters PhD thesis. In this present study, the criterion predicts fracture within the experimental uncertainty window for all levels of pre compression except for 10% pre compression, where fracture is predicted too early (Fig. 35).

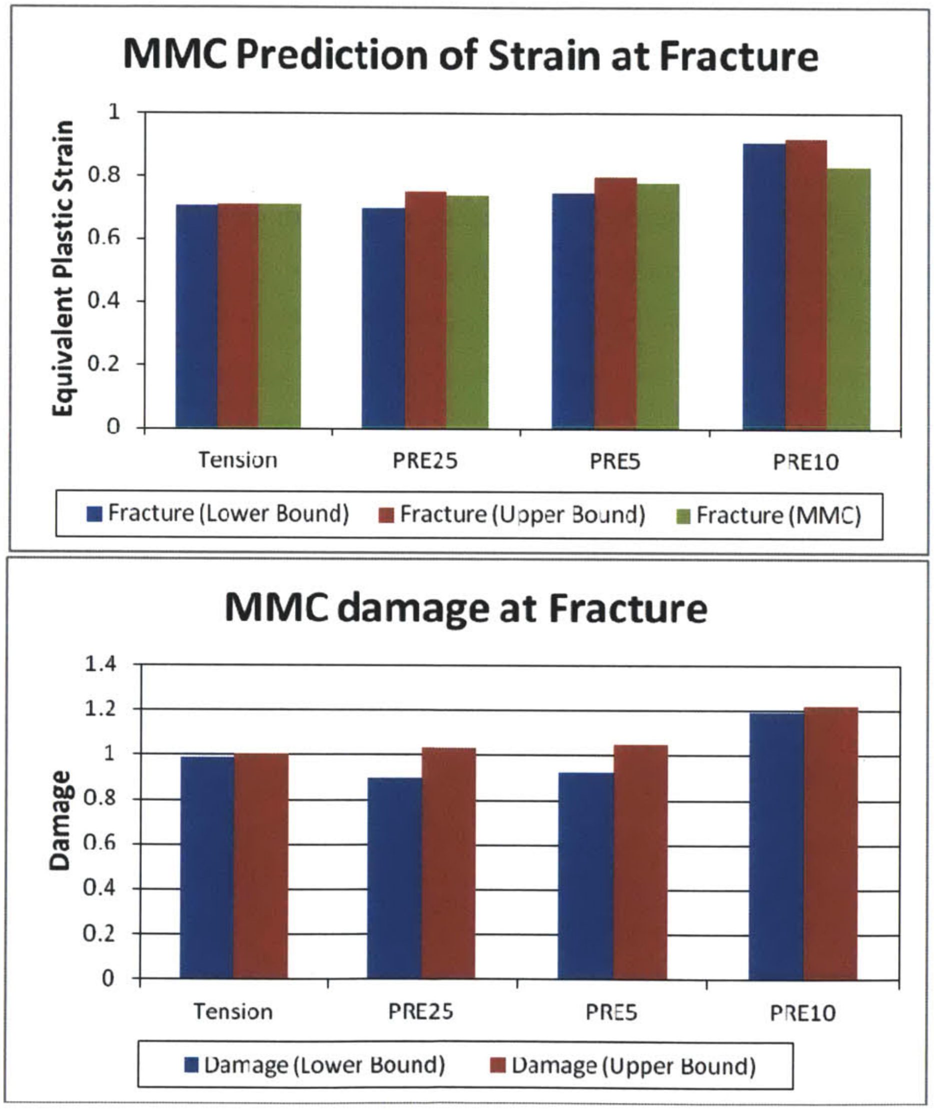

Figure 35 Overview of the prediction of fracture of the Modified Mohr Coulomb Criterion in the case of reversed Loading

4.4 Conclusion

An innovative experimental procedure has been developed to perform large in plane compression on sheet metal. The effect of a reverse loading on ductile fracture is studied. A hybrid experimental and numeric method is necessary to observe the history of local stress and strain state at the fracture locus. A suitable constitutive model is developed and calibrated to be able to predict the behavior of the material in the case of reversed loading. A derivative free optimization method is used to calibrate the plasticity parameters. The model is able to predict accurately the load displacement curves, especially during the necking phase. The transition between elastic and plastic phase is not well predicted but has little impact on the state of stress ans strain at fracture. This study shows that little damage is accumulated in the material during the compression phase and validates phenomenological models that predict little damage accumulation for negative values of the triaxiality.

Chapter 5.

V Conclusion

A hybrid experimental and numerical method to evaluate the history of local stress and strains in the gage section of fracture experiments was presented and validated for a dual-phase steel. A phenomenological fracture criterion was calibrated and validated by using the hybrid method for several innovative tests in order to observe fracture in a wide range of stresses and strains. Local stress and strain paths are found to be non linear after localization of the plastic strain that characterizes necking. A theory of damage accumulation takes this non linear effect into account by integrating the plastic strain weighted by the Modified Mohr Coulomb criterion, which is a function of the triaxiality and Lode angle parameter, two invariants of the stress tensor.

A study of the effect of reverse loading on the ductile fracture in then presented. An innovative experimental procedure is developed to perform in-plane pre-compression followed by uniaxial tension. An anti buckling device and special grips make it possible to delay buckling and reach 15% compression on sheet metal. The hybrid method requires the choice of a suitable constitutive model for the material in the case of reverse loading. A modified Yoshida plasticity model is chosen, and requires a careful calibration of its parameter. The optimization method on the prediction of the load displacement relation uses a Finite Element model. The load displacement curve is still accurately predicted after localized necking. The observation of the history of local stress and strain state reveals that pre-compression has little impact on the stress state at fracture, but that the equivalent plastic strain at fracture increases significantly with increasing pre-compression. Phenomenological ductile fracture models predict that little damage is accumulated at negative values of triaxiality. These tests validate such a prediction.

References

Abaqus, Reference manuals v6.9, Abaqus Inc, 2008.

Armstrong, P.J., Frederick, C.O., 1966. A mathematical representation of the multiaxial Bauschinger effect. Report RD/B/N731, Central Electricity Generating Board, Berkeley, UK.

Bai Y., Effect of Loading History on Necking and Fracture, PhD Thesis, MIT Department of Mechanical Engineering, 2008.

Bai Y, Wierzbicki T, A new model of metal plasticity and fracture with pressure and Lode dependence, Int. J. Plasticity 24, 1071-1096, 2008.

Bai, Y, Wierzbicki, T, Application of extended Mohr–Coulomb criterion to ductile Fracture. Int J Fract (2010) 161:1–20 DOI 10.1007/s10704-009-9422-8

Bao Y, Prediction of Ductile Crack Formation in Uncracked Bodies, PhD Thesis, Ocean Engineering, Massachusetts Institute of Technology, 2003.

BaoY, Wierzbicki T, A comparative study on various ductile crack formation criteria, J. Engrg. Mater. Techn. 126, 314-324, 2004.

Bao Y, Wierzbicki T (2004) On fracture locus in the equivalent strain and stress triaxiality space. Int J Mech Sci 46(1): 81–98

Yingbin Bao, Roland Treitler, Ductile crack formation on notched Al2024-T351 bars under compression–tension loading, Materials Science and Engineering A 384 (2004) 385–394

Barlat F, Brem JC, Yoon JW, Chung K, Dick RE, Choi SH, Pourboghrat F, Chu E, Lege DJ,

Plane stress yield function for aluminum alloy sheets, Int. J. Plasticity 19, 1297, 2003a Barlat F, Ferreira Duarte JM, Gracio JJ, Lopes AB, Rauch EF, Plastic flow for non monotonic loading conditions of an aluminum alloy sheet sample, Int, J. Plastcity 19, 1215, 2003b.

Chaboche JL, A review of some plasticity and viscoplasticity constitutive theories, Int. J. Plast. 24(10), 1642-1693, 2008

Mohr, D., Dunand, M., Kim, K.H., 2010. Evaluation of associated and non-associated quadratic plasticity models for advanced high strength steels sheets under multi-axial loading. Int. J. Plasticity, in press, doi:10.1016/j.ijplas.2009.11.006.

Dunand M and Mohr D, Hybrid Experimental-numerical Analysis of Basic Ductile Fracture Experiments for Sheet Metals, Int. J. Solids Structures, 2009, doi: 10.1016/j.ijsolstr.2009.12.011

Frederick, C.O., Armstrong, P.J., 2007. A mathematical representation of the multiaxial Bauschinger effect. Materials at High Temperatures 24, 11-26.

A.L. Gurson, Plastic flow and fracture behavior of ductile materials incorporating void nucleation, growth and interaction, Ph.D. Thesis, Brown University, 1975.

Gurson AL, Continuum Theory of Ductile Rupture by Void Nucleation and Growth: Part I Yield Criteria and Flow Rules for Porous Ductile Media, J. Eng. Mater. Technol. 99, 2 15, 1977.

Hancock JW, Browm DK, On the Role of Strain and Stress State in Ductile Failure, J. Mech. Phys. Solids 31, 1-24, 1983

Hancock JW, Mackenzie AC, On the Mechanisms of Ductile Failure in High-Strength Steels Subjected to Multi-axial Stress States, J. Mech. Phys. Solids 24, 147-160, 1976.

Hill R, A theory of the yielding and plastic flow of anisotropic metals, Proc. Royal Soc. London A193, pp. 281-297, 1948.

Johnson GR, Cook WH, Fracture Characteristics of three Metals Subjected to Various Strains, Strain Rate, Temperatures and Pressures, Eng. Fracture Mechanics 21, 31-48, 1985

Kuwabara T, Ikeda S, Kuroda T, Measurement and Analysis of differential work hardening in cold-rolled steel sheet under biaxial tension. J. Mater. Process. Technol. 80–81, 517–523, 1998

Kuwabara T, Advances in experiments on metal sheets and tubes in support of constitutive modeling and forming simulations, Int. J. Plast. 23(3), 385-419, 2007

Kuwabara, T., Morita, Y., Miyashita, Y., Takahashi, S., 1995. Elastic-plastic behavior of sheet metal subjected to in-plane reverse loading. In: Tanimura, S., Khan, A.S. (Eds). Proc. 5th Int. Symp. on Plasticity and Its Current Applications, Gordon and Breach Publishers, pp. 841–844.

Lagarias, J.C., J. A. Reeds, M. H. Wright, and P. E. Wright, "Convergence Properties of the Nelder-Mead Simplex Method in Low Dimensions," *SIAM Journal of Optimization*, Vol. 9 Number 1, pp. 112-147, 1998.

Lemaitre, J., Chaboche, J.L., 1994. Mechanics of Solid Materials, Cambridge University Press

McClintock FA, A criterion of ductile fracture by growth of holes, J. Appl. Mech. 35, 363-371, 1968.

F.A. McClintock, Behaviour of Defects at High Temperatures, Mechanical Engineering Publications, London, 1993.

Mohr D, Dunand M, Kim KH, Evaluation of Associated and Non-associated Quadratic Plasticity Models For Advanced High Strength Steels Sheets under Multi-axial Loading, Submitted (Int. J. of Plasticity, December 2008).

Mohr D, Ebnoether F, Plasticity and Fracture of Martensitic Boron Steel under Plane Stress Conditions, Int. J. Solids and Structures 46 (20), 3535-3547, 2009.

Mohr D, Henn S, Calibration of Stress-triaxiality Dependent Crack Formation Criteria: A New Hybrid Experimental-Numerical Method, Experimental Mechanics 47, 805-820, 2007.

Mohr D, Jacquemin J, Large Deformation of Anisotropic Austenitic Stainless Steel Sheets at room Temperature: Multi-axial Experiments and Phenomenological Modeling, J. Mechanics and Physics Sol. 56(10), 2935-2956, 2008.

Mohr D, Oswald M, A New Experimental Technique for the Multi-axial Testing of Advanced High Strength Steels, Experimental Mechanics 48, 65-77, 2008.

Prager, W., 1949. Recent developments in the mathematical theory of plasticity. Journal of Applied Physics 20, 235-241.

Rice JR, Tracey DM. On the ductile enlargement of voids in triaxial stress fields, J. Mech. Phys. Solids 17, 201-217, 1969.

C.S. Seok, Y.J. Kim, J.I. Weon, Nucl. Eng. Des. 191 (1999) 217–224.

Tvergaard V, Needleman A, Analysis of the Cup-Cone Fracture in a Round Tensile Bar, Acta Metall 32, 157-169, 1984.

Walters CL, Effect of strain rate on fracture, PhD Thesis, MIT Department of Mechanical Engineering, 2009.

Wierzbicki T, Xue L, On the Effect of the Third Invariant of the Stress Deviator on Ductile Fracture, Technical Report 136, Impact and Crashworthiness Laboratory, Massachusetts Institute of Technology, 2005.

Yoshida F, Uemori T, Fujiwara K, Elastic-plastic behavior of steel sheets under in-plane cyclic tension-compression at large strain, Int. J. Plasticity 18, 633-659, 2002.

Annex

Effect of non linear loading paths on sheet metal forming limits: large in-plane pre strain followed by uniaxial tension

Summary of the Internship at General Motors, Summer 2011

Light weighting plays a major role in the automotive industry to improve fuel efficiency and reduce greenhouse gas emissions. Advanced High Strength Steels (AHSS) are new materials developed by the steel industry that provide higher strength at a lower weight. The research project I took part in is funded by DOE/USCAR/ASP through the Auto Steel Partnership ASP061: Nonlinear Strain Path Project with team members from GM, Ford, Chrysler, and steel company members. The main goal is to increase the widespread use of AHSS to achieve light-weighting objectives through improved understanding of stress-strain behavior and metal failure mechanisms under nonlinear deformation processes in multi-stage manufacturing and combined manufacturing/product performance simulation. This problem is challenging due to the difficulty to measure local stress and strains in conventional uniaxial tension tests beyond uniform elongation. Different methods to evaluate the forming limit obtained in experimental tests have been considered. The local strain field can accurately be observed with Digital Image Correlation (DIC) after uniform elongation up to a certain level of strain. The actual shape of the surface of the material is observed by using 3D DIC to measure the coordinates of carefully selected points in the direction perpendicular to the surface. An analytic study of the load displacement curve obtained during uniaxial tests shows an opportunity to predict to some extent both the mechanical behavior of the material and its forming limit. A reverse engineering method using Abaqus is considered as being the most accurate, but it requires a time consuming calibration of the behavior of the material. We want to improve simulation of non linear loading conditions that occur in multi-stage forming processes and combined manufacturing/product performance simulations that are beyond the scope of existing material models. The goal is to develop and validate material models of stress-strain behavior specifically for nonlinear strain paths.

The main goal is to develop and provide tools that enable engineers to determine the formability of metal sheets using computer simulation. More specifically, improvements are sought of the simulation of non linear loading conditions that occur in multi-stage forming processes and combined manufacturing/product performance simulations that are beyond the scope of existing material models. Material models of stress-strain behavior specifically for nonlinear strain paths have not been developed and validated due to the inability to measure local stress and strains in conventional uniaxial tension tests beyond uniform elongation. Forming limits under nonlinear strain paths are not well understood and models currently used in engineering are known to be unreliable in nonlinear forming conditions.

Forming limits of complex parts are nowadays predicted with computer simulation. In most situations, highly non linear strain paths are involved when forming complex parts. The material models currently used by engineers are proved to be unreliable in nonlinear forming conditions. Some of the reasons are that engineers make use of Strain based criterion for forming limits (strain path dependant), isotropic hardening (No loading history), and shell elements (Poor prediction of localization of deformation in the third direction).In addition, the automotive industry lacks experience with and good experimental data for forming limits of most AHSS (Advanced High Strength Steels). In these conditions, the purpose of the present project is to understand the effect of non linear strain paths on forming limits and fracture, increase the amount of experimental data for forming limits of AHSS and improve simulations beyond the scope of existing material models.

To understand the effect of pre strain on ductile fracture, General Motors made a partnership with Ockland University to perform uniaxial tension tests of pre strained specimens. Over 600 tests were performed using DIC (Digital Image Correlation) strain measurement system. Seven materials were tested, including DP 600, DP 780, DP 980, and TRIP 780. The different pre strain conditions included Equibiaxial and three directions of uniaxial pre-strain up to three levels. Then, uniaxial tension tests were performed to failure in seven directions after each of the above pre strains. I had several responsibilities as part of this project: (i) analyze data to obtain conventional material properties (ii) characterize the change of these properties with strain (iii) develop reverse engineering and other analytical techniques using DIC data to extend stress-strain relations beyond maximum load (iv) finally develop analytical techniques to estimate necking and fracture limits and document how they are affected by nonlinear deformation. The main contribution I made was to develop an automatic Matlab code to post process all Data from 600 tests to determine standard material properties and how they change with deformation. In addition to this, I also developed several criteria to determine the onset of localized necking. The first criterion is an analytic model using a maximum load per unit thickness. Localized necking can also be observed visually thanks to digital image correlation technology. Inspired from the two methods above, a combined method with analytic solution and DIC using maximum local true stress has also been introduced. The most reliable method, but also the most expensive in terms of computation time, remains the Reverse Engineering method using Finite Element Analysis. It requires a fine calibration of the material behavior. These criteria have been compared, their accuracy has been evaluated, and their reliability assessed.

Material models of stress-strain behavior specifically for nonlinear strain paths have not been developed and validated due to the inability to measure local stress and strains in conventional uniaxial tension tests beyond uniform elongation. Digital Image Correlation is used to measure local strains directly on the surface of the specimen. Two Cameras record the deformation of the painted surface, allowing an analysis of the deformation of the surface in three dimensions. In order to enable the digital image correlation measurements, the surface of the specimens are painted. First, a thin layer of white paint is applied. Then a pattern of black paint speckles is sprayed on the specimens. The typical size where strains are measured is of the order of a millimeter. The main issue is that the width of the localized necking is also expected to be of the order of the millimeter (thickness of the sheet). Therefore, it has been pointed out during the project that DIC strain measurements are not local enough to identify high strains after localized necking. Nevertheless, 2D DIC allows us to observe severe localization of deformation after diffused necking. But this method does not show the expected magnitude of strains for localized necking. On the other hand, 3D DIC gives an opportunity to detect the localized deformation in the thickness. Unfortunately, a very high noise is observed in the measurement of the thickness to due camera precision and material roughness.

The typical length scale of an element is four times smaller than the subset used in the DIC method, but he expected scale of the necking area is that of the DIC measurement, therefore the simulation gives much better strain prediction after necking. The reverse engineering method consists in trying to match the simulated load displacement curve with the experimental one by modifying and optimizing the behavior of the material. We assume that the material behavior that enables us to match curve is an accurate description of the material. An anisotropic yield surface (Hill) is calibrated from experiments. The FEA simulation predicts much higher local strains than observed with DIC. The main strength of such a method is that all required information can be extracted from such an analysis, as all local stresses and strains are available. But the Reverse Engineering method is highly time-consuming, as the stress strain behavior has to be recalibrated for every test. To avoid calibration and save computation time, a unique and more complex model has to be developed and calibrated, including: anisotropy, advanced hardening models (Isotropic, kinematic…), and a choice between associated and non associated flow rules.

To familiarize the automotive industry with forming limits of most AHSS and acquire a significant amount of good experimental data, I had the responsibility to perform and analyze Marciniak tests on a high strength steel (TRIP780). Due to a deformation induced transformation from ductile austenite to high strength martinsite steel, TRIP steels show considerable opportunity for light-weighting complex product shapes. The forming limits of TRIP steel are known to be highly anisotropic, yet among the least well documented. To characterize the shape of the forming limit in strain space, eight shapes of specimens were used. And to characterize the anisotropy of the forming limit, they were cut in three different directions with respect to rolling direction. Each test has been repeated in order to be able to interrupt loading at different stages of the localized necking phase so that both necking and fracture limits can be accurately documented. During the internship, 41 tests were performed. First, fracture tests for each shape and each material direction were performed. According to the fracture limits determined from this first set of tests, interrupted tests to onset of necking in the rolling direction have been performed for six types of shapes. It was particularly interesting to observe anisotropic fracture on some shapes of specimens. We also obtained various stages of localized necking. Part of my responsibility was also to Process DIC data to extract strain history in region of neck and fractures.

Strain path for several pre strained tension tests.

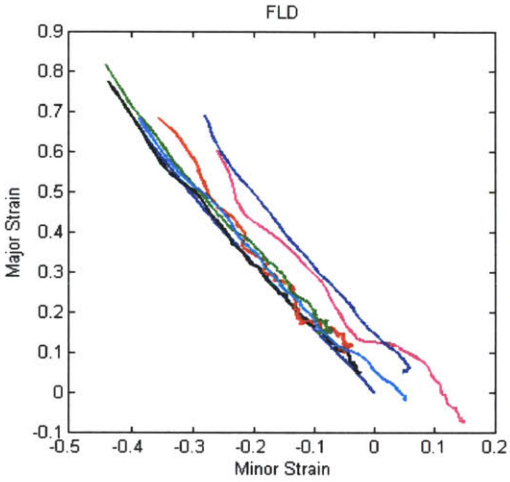

DIC strain measurements after necking.